

LOW-MASS GALAXY FORMATION IN COSMOLOGICAL AMR SIMULATIONS: THE EFFECTS OF VARYING THE SUB-GRID PHYSICS PARAMETERS

PEDRO COLÍN¹ VLADIMIR AVILA-REESE², ENRIQUE VÁZQUEZ-SEMADENI¹, OCTAVIO VALENZUELA², AND DANIEL CEVERINO³

¹ Centro de Radioastronomía y Astrofísica, Universidad Nacional Autónoma de México, A.P. 72-3 (Xangari), Morelia, Michoacán 58089, México

² Instituto de Astronomía, Universidad Nacional Autónoma de México, A.P. 70-264, 04510, México, D.F., México

³ Racah Institute of Physics, The Hebrew University, Jerusalem 91904, Israel

Draft version June 15, 2018

ABSTRACT

We present numerical simulations aimed at exploring the effects of varying the sub-grid physics parameters on the evolution and the properties of the galaxy formed in a low-mass dark matter halo ($\sim 7 \times 10^{10} h^{-1} M_{\odot}$ at redshift $z = 0$). The simulations are run within a cosmological setting with a nominal resolution of 218 pc comoving and are stopped at $z = 0.43$. For simulations that cannot resolve individual molecular clouds, we propose the criterion that the threshold density for star formation, n_{SF} , should be chosen such that the column density of the star-forming cells equals the threshold value for molecule formation, $N \sim 10^{21} \text{ cm}^{-2}$, or $\sim 8 M_{\odot} \text{ pc}^{-2}$. In all of our simulations, an extended old/intermediate-age stellar halo and a more compact younger stellar disk are formed, and in most cases, the halo's specific angular momentum is slightly larger than that of the galaxy, and sensitive to the SF/feedback parameters. We found that a non negligible fraction of the halo stars are formed in situ in a spheroidal distribution. Changes in the sub-grid physics parameters affect significantly and in a complex way the evolution and properties of the galaxy: (i) Lower threshold densities n_{SF} produce larger stellar effective radii R_e , less peaked circular velocity curves $V_c(R)$, and greater amounts of low-density and hot gas in the disk mid-plane; (ii) When stellar feedback is modeled by temporarily switching off radiative cooling in the star forming regions, R_e increases (by a factor of ~ 2 in our particular model), the circular velocity curve becomes flatter, and a complex multi-phase gaseous disk structure develops; (iii) A more efficient local conversion of gas mass to stars, measured by a stellar particle mass distribution biased toward larger values, increases the strength of the feedback energy injection –driving outflows and inducing burstier SF histories; iv) If feedback is too strong, gas loss by galactic outflows –which are easier to produce in low-mass galaxies– interrupts SF, whose history becomes episodic; v) In all cases, the surface SF rate versus the gas surface density correlation is steeper than the Kennicutt law but in agreement with observations in low-surface brightness galaxies. The simulations exhibit two important shortcomings: the baryon fractions are higher, and the specific SF rates are much smaller, than observationally inferred values for redshifts $\sim 0.4 - 1$. These shortcomings pose a major challenge to the SF/feedback physics commonly applied in the Λ CDM-based galaxy formation simulations.

Subject headings: cosmology:dark matter — galaxies:formation — galaxies:haloes — methods: N -body simulations

1. INTRODUCTION

The successful development of cosmology in the last two decades, incarnated in the popular Λ CDM model, has provided a robust theoretical background for modeling galaxy formation and evolution (for reviews see Baugh 2006; Avila-Reese 2007). Due to the high non-linearity implied in the problem, cosmological N -body + hydrodynamical simulations offer the fairest way to attain such a modeling (for a recent review see Mayer et al. 2008). However, this method is hampered by the large –currently unreachable– dynamic range required to model galaxy formation and evolution in the cosmological context (formally from the subpc scales of molecular cloud cores to Mpc scales, and from densities $n \sim 10^{-6}$ to $\gtrsim 10^2 \text{ cm}^{-3}$), as well as by the complexity of the processes involved, mainly cooling and star formation (SF) and its feedback on the surrounding medium. Both of them occur at scales com-

monly well below the accesible resolution in simulations. Theoretical and observational results suggest that the star formation efficiency can be simulated without reaching the subparsec resolution if a simulation can resolve the mean density of giant molecular clouds (Gnedin et al. 2009; Krumholz & McKee 2005), unfortunately this seems not to be the case for SN and Stellar Wind feedback. Undoubtedly, modeling of SF and feedback (subgrid physics) is of crucial importance for the simulations of galaxy formation and evolution.

On the other hand, the SF rate (SFR) and its evolution are among the most important observational properties of galaxies, being basically responsible for coining the present-day galactic stellar populations. Star formation is also crucial in terms of its feedback effect, which (i) regulates several thermo- and hydro-dynamical processes of the multi-phase ISM, including probably the SF itself; (ii) partially controls the galaxy assembly process through mass outflows and re-heating of the circumgalactic medium, and (iii) likely is also the driving agent of

the intergalactic chemical enrichment.

In the context of the hierarchical Λ CDM scenario, the efficient radiative cooling of gas leads to the so-called ‘‘gas cooling catastrophe’’: most of the available primordial gas is cooled, trapped, and transformed into stars inside the smallest, early-collapsing halos (White & Rees 1978). In order to avoid such a problem, the stellar negative feedback is routinely invoked (see for recent works e.g., Okamoto et al. 2005; Zavala et al. 2008, though alternative physical processes have been also considered, e.g., Sommer-Larsen & Dolgov 2001; Governato et al. 2004). In the same vein, it is well known now that the mass fraction of baryons in galaxies with respect to their halo masses is much smaller than the universal baryon fraction $f_b = \Omega_b/\Omega_0$. The ‘missing baryons’ are commonly assumed to have been expelled from galaxies by feedback effects, especially in the past, when the halos were smaller (Dekel & Silk 1986).

In the absence of a general theory of SF and feedback, several prescriptions have been proposed in order to model the corresponding subgrid physics in numerical simulations at parsec scales or smaller, with the aim to properly extend SF/feedback influence into the larger (tens/hundreds of parsecs) resolved scales. Unavoidably, subgrid SF and feedback prescriptions in simulations introduce several free parameters.

In simulations, some of the common criteria used for declaring a gas cell or particle as star forming are converging cold gas flows, a local Jeans instability and/or a local gas density threshold (n_{SF}) (see e.g., Katz et al. 1996; Kravtsov et al. 2003). The rate at which the gaseous mass element obeying the above criteria is converted into ‘stars’ is calculated using recipes which introduce some free parameters like the SF efficiency constant C_* (e.g., Katz 1992; Navarro & White 1993; Gerritsen & Icke 1997; Springel & Hernquist 2003). In order to take into account the stochastic nature of gas conversion into stars, and also the fact that the minimum resolution element overlooks local variations in gas density, a probabilistic function around n_{SF} is typically introduced instead of a deterministic density criterion (e.g., Stinson et al. 2006).

For the modeling of the feedback processes associated to the non-resolved regions, in which they start to operate, two schemes are commonly used: individual gas elements surrounding a stellar particle are given a velocity kick (kinematic feedback; e.g., Navarro & White 1993; Abadi et al. 2003; Dubois & Teyssier 2008) and/or are injected with thermal energy and metals (e.g., Kravtsov et al. 2003), at the same time that, in some schemes, the radiative cooling is temporarily turned off to prevent the thermal energy from being radiated away before it is converted into kinetic energy (adiabatic feedback; e.g., Gerritsen & Icke 1997; Thacker & Couchman 2000; Stinson et al. 2006). Alternatively, in other schemes, the interaction between neighbor particles belonging to different phases is inhibited by hand (Okamoto et al. 2003; Scannapieco et al. 2006). A third scheme, often applied, imposes an effective gas equation of state in order to describe the unresolved multiphase ISM (e.g., Yepes et al. 1997; Springel & Hernquist 2003). Hybrid schemes were also used: semi-analytical models of winds and starbursts dependent on the gas physical conditions are included in the

simulations (Springel & Hernquist 2003). In all these feedback schemes there are free parameters, such as the amounts of momentum and thermal energy deposited into the gas elements, the time the cooling is switched off, t_{off} , etc.

The values for the free parameters in the SF and feedback prescriptions are chosen in different ways. They can be defined *a priori*, based on constraints typically related to observations of the Galaxy ISM, and/or *a posteriori*, choosing the parameter values that make the evolution and properties of the simulated galaxy close to the observed ones. The prescriptions and parameters used also depend on whether the code is of the smoothed particle hydrodynamics (SPH) or Eulerian adaptive mesh refinement (AMR) kind.

Because of the large diversity of models, strategies, and relevant parameters of SF/feedback implementations, a comparison between them is not trivial. Although some implementations in high-resolution simulations have reached an amount of success forming rotational supported disk galaxies (see, for recent reviews, Mayer et al. 2008; Gibson et al. 2009, and references therein), the task is far from being completed. It is not clear what are the quantitative differences between each subgrid model. Thus, a characterization of the various subgrid schemes for the ISM energy injection and dissipation is needed to gain some insight into their ability/inability to form disk galaxies.

In this paper, we explore the effects of the SF/feedback parameters on the structure and evolution of a *low-mass galaxy* in cosmological simulations using the Hydrodynamics Adaptive Refinement Tree (ART) code (Kravtsov et al. 1997, 2003). We reach a maximum resolution of about one hundred parsecs at redshift $z = 1$ in order to be able to resolve the clouds associated with the SF; most of our analysis is made at this epoch and at $z = 0.43$, the last epoch reached by all the runs. Our nominal resolution extrapolated to $z = 0$ is of 218 pc, which is among the highest resolutions for a cosmological galaxy formation experiment using the AMR/Eulerian technique (c.f. Gibson et al. 2009).

We will focus our analysis on general evolutionary and physical properties/processes of the simulated galaxies, namely: (i) the evolution of structural and dynamical properties (e.g., galaxy stellar structure, circular velocity curve decomposition), (ii) the structure/thermodynamics of the ISM (density and temperature probability distribution functions, vertical filling factors of the different phases of the ISM, gas fractions), (iii) the dependence of the global SF history and the SFR on gas density, and (iv) global quantities like the baryon mass and angular momentum fractions. Our aim here is not to simulate galaxies that can be compared to observations, but rather to determine the effects of the parameters of the SF/Feedback prescriptions. Moreover, we will use our results to point out some potential difficulties of simulated low-mass galaxies in the context of the Λ CDM cosmogony.

The plan of the paper is as follows. The code and the SF and feedback prescriptions used for the simulations are described in §2. In this section, the cosmological simulation and the different runs varying the SF/feedback parameters are also presented. The results of the various runs are given and compared with each other in §3. In

§4 we present a summary of the main results obtained in the paper accompanied by interpretations and discussions. Some potential vexing problems of any Λ CDM-based model of low-mass galaxy formation and evolution are highlighted in §4.3. Finally, our conclusions are given in §5.

2. NUMERICAL EXPERIMENTS

2.1. *The Code*

The numerical simulations described here were performed using the hydrodynamics + N-body Adaptive Refinement Tree code ART (Kravtsov et al. 1997, 2003). Among the physical processes included in the code are the cooling of the gas and its subsequent conversion into stars, stellar feedback, self-consistent advection of metals, an UV heating background source, etc.

The cooling and heating rates incorporate Compton heating/cooling, atomic and molecular cooling, UV heating from a cosmological background radiation (Haardt & Madau 1996), and are tabulated for a temperature range of $10^2 < T < 10^9$ K and a grid of densities, metallicities, and redshifts using the CLOUDY code (Ferland et al. 1998, version 96b4). Gas is converted into stellar particles according to a prescription described and discussed below. Stellar particles eject metals and thermal energy through stellar winds and type II and Ia supernovae explosions. Each supernova dumps 2×10^{51} ergs of thermal energy and ejects $1.3M_{\odot}$ of metals. For the assumed Miller & Scalo (1979) initial mass function, IMF, a stellar particle of $10^5 M_{\odot}$ produces 749 type II supernovae. For a more detailed discussion of the processes implemented in the code, see Kravtsov et al. (2003, 2005).

2.2. *Star formation and feedback*

In ART, SF is modeled as taking place in the coldest and densest collapsed regions, defined by $T < T_{\text{SF}}$ and $\rho_g > \rho_{\text{SF}}$, where T and ρ_g are the temperature and density of the gas, respectively, and ρ_{SF} is a density threshold. A stellar particle of mass m_* is placed in a grid cell where these conditions are simultaneously satisfied, and this mass is removed from the gas mass in the cell. The particle subsequently follows N-body dynamics. No other criteria are imposed.

Although n_{SF} , the hydrogen number density threshold corresponding to ρ_{SF} , is in principle a free parameter of the simulations, one can make an “educated guess” as to which values should be considered most realistic, by noting that SF occurs almost exclusively in giant molecular clouds (GMCs). Thus, it is natural to require that the density in a star-forming cell should be at least such that the cell’s column density equals the threshold value for molecular Hydrogen and CO formation, $N \gtrsim 10^{21} \text{cm}^{-2}$ (Franco & Cox 1986; van Dishoeck & Black 1988). For a cell of 150 pc, this translates into a number density $n_{\text{SF}} \sim 5 \text{cm}^{-3}$. In our models, n_{SF} is varied around this value from 0.1 to 50cm^{-3} . We keep T_{SF} fixed at 9000 K.

The stellar particle mass, m_* , is determined through a simple two-step process. A first estimate of this mass, labeled m_1 , is made by assuming that m_* is proportional to a power law of the gas density, ρ_g^α . In this work we use $\alpha = 1.0$. Thus, in this step, collisionless stellar particles

can be created with a mass $m_1 = C_* m_{\text{gas}} dt_0$, where C_* is a constant that measures the “efficiency” with which gas is locally converted into stars during dt_0 , the time step of the coarsest grid, which is also the time interval between successive checks by the code for the formation of new stellar particles; m_{gas} is the gas mass in the cell. For low values of C_* , for example $C_* = 2.5 \times 10^{-10} \text{yr}^{-1}$ (the fiducial value in the code), the formula above produces small m_1 values. However, this makes the number of stellar particles in the simulation practically intractable. For this reason, a stellar particle mass limit is introduced in the SF set of parameters, labeled $m_{*,\text{lim}}$. The SF algorithm then chooses the maximum between m_1 and $m_{*,\text{lim}}$, which we call m_2 . In the second step, the algorithm takes the minimum between m_2 and $2/3$ of the gas mass contained in the cell and assigns this mass to the stellar particle, in order to prevent total exhaustion of the gas contents of the cell. Since the stellar particle masses are much more massive than the mass of a star, typically $10^4 - 10^5 M_{\odot}$, once formed, each stellar particle is considered as a single stellar population, within which the individual stellar masses are distributed according to the Miller & Scalo IMF.

The simulations reported here are of two kinds: those with a “deterministic” SF prescription (the “D” runs), in which stellar particles are always created once the density and temperature conditions are satisfied, and those with a “stochastic” or “random” SF prescription (the “R” runs), in which stellar particles are created in a cell with a probability given by

$$P = \begin{cases} 0 & \text{if } \rho_g < \rho_{\text{SF}}; \\ \frac{\rho_g}{\beta \rho_{\text{SF}}} & \text{if } \rho_{\text{SF}} < \rho_g < \beta \rho_{\text{SF}}; \\ 1 & \text{if } \beta \rho_{\text{SF}} < \rho_g. \end{cases} \quad (1)$$

where β is a free parameter, to which we refer as the probability-saturation threshold. Thus, regions with higher densities have higher probabilities to host SF events. This stochastic prescription allows for the possibility of forming stars in regions of low average density (assuming we have chosen a low n_{SF} parameter), in which isolated dense clouds would not be resolved.

The runs can also be divided in two classes according to the stellar feedback implementation. In the first class of runs, all the energy from stellar feedback is dumped onto the star-forming cell in the form of heat, as described, for example, in Kravtsov et al. (2003). This thermal feedback suffers from the well-known overcooling problem in low-resolution simulations. This problem can be traced back to insufficient numerical resolution (Ceverino & Klypin 2009), and happens when the characteristic expansion time in a cell heated by a stellar particle (given by the sound crossing time across the cell) is much longer than the cooling time at high densities and low resolutions (large cell size). In this case, in a single timestep, the gas cools before it has time to expand. The resolution condition to avoid this problem would then be to require that the sound crossing time across the cell be shorter than the local cooling time. This, however, can require impossibly high resolutions with presently available computational resources.

A frequent strategy to overcome this problem (e.g., Gerritsen & Icke 1997; Thacker & Couchman 2000; Sommer-Larsen et al. 2003; Kereš et al. 2005;

Governato et al. 2007) is to turn off the cooling in a cell for some time after a stellar particle is produced there, in order to allow for the gas to expand before it cools. Although this procedure has been criticized as being somewhat arbitrary and unrealistic (e.g., Ceverino & Klypin 2009), we consider that it is physically motivated, as it is even more unrealistic to prevent the expansion of heated regions due to the inability to resolve the scales that would allow the physically correct behavior of these regions. In the present paper we therefore adopt this strategy, and test its effects on the evolution of the forming galaxy. Specifically, we turn off the cooling in a cell for 40 Myr after a SF event occurs there in some of the runs (see Table 1).

2.3. The numerical method

We present here several simulations of the evolution of a galaxy with a total (baryon + dark matter) mass of about $7 \times 10^{10} h^{-1} M_{\odot}$ at the present day. The analysis is made at two epochs, $z = 1$ and $z = 0.43$. The latter corresponds to a time just before the last major merger. The simulations are run in a Λ CDM cosmology with $\Omega_0 = 0.3$, $\Omega_{\Lambda} = 0.7$, and $\Omega_b = 0.045$. The CDM power spectrum is taken from Klypin & Holtzman (1997) and it is normalized to $\sigma_8 = 0.8$, where σ_8 is the rms amplitude of mass fluctuations in $8 h^{-1} \text{Mpc}$ spheres.

To maximize the resolution efficiency, we first perform a low-resolution N-body simulation with 128^3 dark matter (DM) particles in a periodic box of $10 h^{-1} \text{Mpc}$ on a side. At the start of the simulation, the box is initially covered by a mesh of 128^3 cells (zerth level cells). A spherical region, centered on a *randomly* selected halo of mass $2.6 \times 10^{11} h^{-1} M_{\odot}$ and with a radius equal to three times the virial radius (R_{vir}) of the halo, was then chosen at $z = 0$ and its corresponding Lagrangian region, identified at $z = 50$, was re-sampled with additional small-scale modes (Klypin et al. 2001). The virial radius is defined as the radius that encloses a mean density equal to Δ_{vir} times the mean density of the universe, where Δ_{vir} is a quantity that depends on Ω_0 , Ω_{Λ} and z . For example, for our cosmology $\Delta_{\text{vir}}(z = 1) = 203$. The number of DM particles in the high-resolution zone is about one million and the mass per particle (m_{dm}) is $5.3 \times 10^5 h^{-1} M_{\odot}$.

In ART, the initially uniform grid is refined recursively as the matter distribution evolves. The criterion chosen for refinement is based on gas or dark matter densities. The cell is refined when the mass in DM particles exceeds $1.3(1 - f_b)m_p$ or the mass in gas is higher than $13.0 f_b m_p$, where $m_p = m_{dm}/(1 - f_b)$. For the simulations presented in this paper, using multiple dark matter particle masses, the grid is always unconditionally refined to the third level, corresponding to an effective grid size of 512^3 . On the other hand, the maximum allowed refinement level l_{max} was set to 9. At $z = 1$, the number of grid cells, at all levels of resolution, is about 11 million. In particular, at l_{max} the number of cells is $\sim 5 \times 10^5$, corresponding to a resolution of 218 comoving parsecs.

In this paper, we focus our study on the third most massive halo appearing in the re-sampled simulations at $z = 1$ because it turns out that it evolves from $z \sim 2$ to $z \sim 0.4$ in a nearly isolated fashion. This allow us to observe the effects that the SF and feedback prescriptions have on the structure and evolution of the embedded galaxy without having to deal with complicated dy-

namical interactions. This halo contains within its virial radius $\sim 10^5$ DM particles at $z = 0$. In the remainder of the paper, we study the properties of this system as a function of the SF/feedback prescriptions and the corresponding parameter values.

2.4. The runs

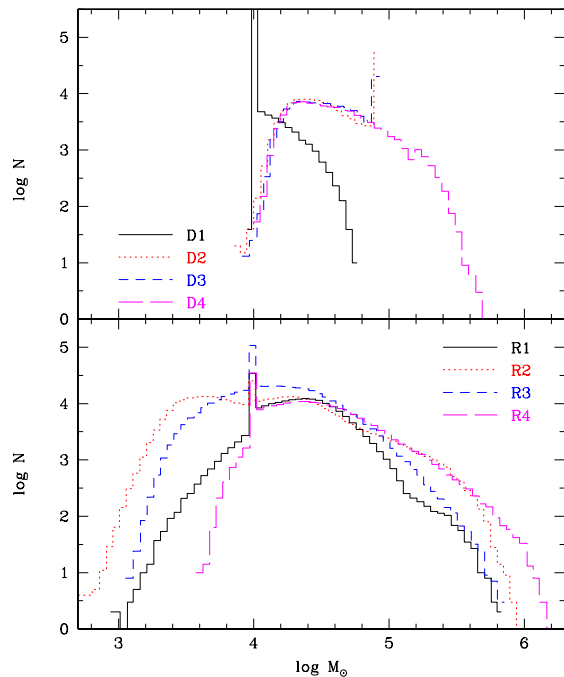


FIG. 1.— Stellar particle mass distributions measured at $z = 1.0$ for all simulations presented in Table 1. The distribution depends on the values of the SF parameters $m_{*,\text{lim}}$, C_* , and n_{SF} .

In Table 1 we list the parameters described above for the various runs we performed. The first column gives the name of the run, denoted by a capital letter followed by a number, where the former indicates whether the SF model belongs to the D or R sequence (see §2.2). In columns (2), (3), and (4) we show the values of $m_{*,\text{lim}}$, n_{SF} , and C_* , respectively. Column (5) indicates whether cooling is always on or it is turned off for 40 Myr after SF events in the simulation. The parameter β , defined above (see eq. 1), is shown in column (6). We also ran an adiabatic simulation. This is denoted in Table 1 by the name Ad (see last row).

The SF scheme and the different values of the SF parameters $m_{*,\text{lim}}$, n_{SF} , and C_* produce different distributions for the stellar particle masses, m_*^1 . Figure 1 shows this distribution at $z = 1.0$ for each of the runs presented in Table 1. Some features can be highlighted from this figure: (a) the distributions of the R sequence of runs are wider than the corresponding distributions of the D sequence. This just reflects the fact that the recipe for SF for the former case is probabilistic; that is, stellar particles can be produced from a wide range of cold gas density values. (b) In most runs the distributions have

¹ These masses refer to the *initial* masses with which stellar particles were born. At later times, the masses are always lower than the initial (original) masses because stellar particles loose mass due to stellar winds and supernova events

TABLE 1
PARAMETER SIMULATIONS

Model	$m_{*,\text{lim}}^{\text{a}}$ ($10^4 M_{\odot}$)	n_{SF}^{b} (cm^{-3})	C_*^{c} ($2.5 \times 10^{-10} \text{ yr}^{-1}$)	Cooling ^d	β^{e} (10^6 yr)
D1	1.0	50.0	1.0	on	off
D2	8.0	6.25	1.0	on	off
D3	8.0	6.25	1.0	40	off
D4	∞	6.25	none	40	off
R1	1.0	1.0	667.0	on	100.0
R2	1.0	0.1	500.0	40	20.0
R3	1.0	1.0	500.0	40	20.0
R4	1.0	6.25	500.0	40	20.0
Ad	off	off	off	off	off

NOTE. — Runs are denoted with the capital letters D or R followed by a number. D stands for deterministic and R for random. The adiabatic run is denoted by Ad. This simulation does not include radiative cooling.

^a Stellar particle mass limit.

^b Threshold gas density for star formation.

^c Star formation efficiency constant.

^d Cooling is always on or turned off for 40 Myr after SF events.

^e Probability-saturation threshold.

a spike at their corresponding $m_{*,\text{lim}}$ value. (c) From series D, run D4 is the one with the largest values of m_* . In this run, where $m_{*,\text{lim}}$ is set to infinite, m_* is always equal to 2/3 the gas mass in the cell. (d) Run R2 has the widest distribution and, along with run R4, it shows the largest values of m_* . Below, we briefly discuss the characteristics of each run.

Run D1 has $m_{*,\text{lim}} = 10^4 M_{\odot}$, $n_{\text{SF}} = 50$, and the cooling is always on (see Table 1). The masses of stellar particles vary from about $10^4 M_{\odot}$ to $6 \times 10^4 M_{\odot}$ and peak at $10^4 M_{\odot}$. This run has the highest density threshold and, along with run R4, the most peaked circular velocity curve (see §3.2).

Run D2 was performed to test the effect of a lower density threshold, although this necessarily implies that more stellar particles will form. We thus increased the value of $m_{*,\text{lim}}$ from $10^4 M_{\odot}$ to $8 \times 10^4 M_{\odot}$ in order to keep the number of stellar particles computationally tractable. Both of these models have a low C_* value but $m_{*,\text{lim}}$ is higher in model D2. This means that, in practice, in this model, in the first step of the SF prescription, $m_2 = m_{*,\text{lim}}$ always (see §2.2). Note, however, that if $m_2 = m_{*,\text{lim}}$ then the final chosen mass of the stellar particle cannot be higher than $m_{*,\text{lim}}$. Thus, in model D2 the masses of stellar particles are restricted to be lower than $8 \times 10^4 M_{\odot}$.

Run D3 is similar to D2 but here we turn off the cooling for 40 Myr after SF events. Run D4 is similar to D3 but here $m_{*,\text{lim}} = \infty$, which means that cells always form stellar particles with a 2/3 efficiency factor (see §2.2); that is, in any SF event, 2/3 of the gas mass in the cell is converted into stars. The masses of the stellar particles vary from about $10^4 M_{\odot}$ to $4 \times 10^5 M_{\odot}$. This model is expected to have a higher impact, as compared with models D2 and D3, on the ISM properties of the simulated galaxy due to the formation of more massive stellar particles, which are concentrated sources of high energy injection.

Aside from $m_{*,\text{lim}}$ and n_{SF} , the R sequence of models include the β parameter (see eq. 1). In model R1 this parameter is 100 while in the rest it is 20; model R1 also differs from the rest in that it includes “runaway stars”

(Ceverino & Klypin 2009), stellar particles able to inject energy to the ISM in regions of low-density gas. In this simulation, which uses a different version of the code, a random velocity, drawn from an exponential distribution with a characteristic scale of 35 km s^{-1} , is added to the inherited gas velocity to 30% of the stellar particles (see Ceverino & Klypin 2008 for more details). We used a characteristic velocity twice higher than the one used by Ceverino & Klypin, whose value was motivated by observations, to take into account the fact that our simulations are twice less resolved. The masses of stellar particles in the R runs vary from about $10^3 M_{\odot}$ to $10^6 M_{\odot}$. Runs R2, R3 and R4 differ only in the value of n_{SF} . All have $m_{*,\text{lim}} = 10^4 M_{\odot}$, $\beta = 20.0$, and the cooling switched off for 40 Myr after SF events. They were run to investigate the effect of varying n_{SF} on the structural and evolutionary properties of the simulated galaxy in the stochastic SF scheme.

3. RESULTS

As mentioned above, our study focuses on the third most massive halo found at $z = 1$ because this halo evolves without significant mergers, at least in the redshift range from $z \sim 2$ to ~ 0.4 . Most of the analysis of the embedded galaxy is performed at two epochs: $z = 1$ and 0.43; for the cosmological model used here, the time interval between these two redshifts is 3.2 Gyr.

Some global properties of the halo in the adiabatic simulation, at different redshifts, are presented in Table 2. Column (4) shows the concentration of the halo as defined by $c_{\text{vir}} = R_{\text{vir}}/r_s^2$. The virial mass of the halo and the specific angular momentum are given in columns (2) and (6), respectively. The baryonic fraction within R_{vir} is presented in column (3) (see also Table 3). Column (4) shows the spin parameter of the halo as defined by (Bullock et al. 2001)

$$\lambda = \frac{J}{\sqrt{2}M_{\text{vir}}V_{\text{vir}}R_{\text{vir}}}, \quad (2)$$

² To obtain r_s , the halo DM density profile was fitted with the NFW profile (Navarro, Frenk, & White 1997).

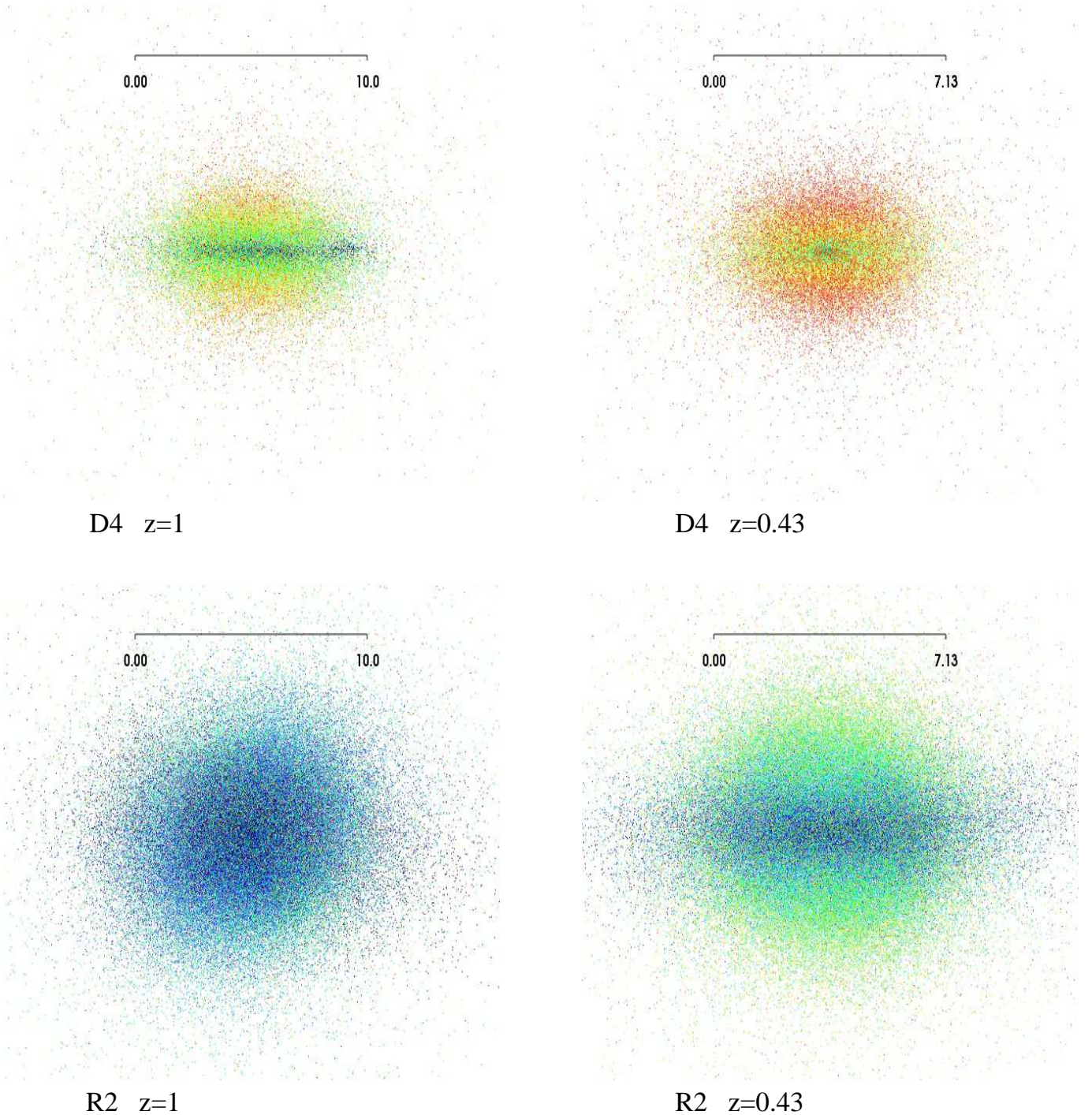


FIG. 2.— Spatial distribution of stellar particles for runs D4 and R2 at $z = 1$ and $z = 0.43$; the disks, when present, are shown edge-on. Scale is comoving $h^{-1}\text{kpc}$ (solid line measures $10 h^{-1}\text{kpc}$). Particles are color coded by age with a rainbow palette with the bluest particles being the youngest ones. At $z = 1$ in run D4 a young stellar disk can be clearly distinguished while in run R2 the young stellar particles are distributed in a spheroid.

where J is the angular momentum inside the halo virial radius, and V_{vir} is the circular velocity at R_{vir} . Moreover, column (2) of Table 3 reports the virial masses of the DM halo in the other runs. At $z = 1$, M_{vir} varies between 4.7 and $5.0 \times 10^{10} M_{\odot}$, while at $z = 0.43$, it varies between 5.4 and $6.6 \times 10^{10} M_{\odot}$. In the following, we will discuss the dependence of the galaxy morphology, stellar populations, dynamics, ISM properties, and SF history of the studied galaxy on the relevant parameters of the

SF and feedback prescriptions.

3.1. Morphology and structure

The different combinations of the parameters used in the SF and feedback prescriptions, described in §2.4, produce a large diversity of galaxy morphologies and stellar populations. As an example, in Fig. 2 we show the stellar spatial distribution for runs D4 and R2 at $z = 1$ and $z = 0.43$, with the disk, when present, seen edge-on.

TABLE 2
ADIABATIC HALO GLOBAL PARAMETERS

z	M_{vir} ($10^{10} M_{\odot}$)	$f_{\text{gal}}(R_{\text{vir}})^{\text{a}}$	c_{vir}	λ	J/M^{b} ($\text{km s}^{-1} \text{kpc}$)
0.0	8.6	0.14	18.4	0.044	285.1
0.4	5.7	0.14	13.4	0.049	212.4
1.0	4.8	0.14	8.0	0.060	202.8

^a Baryon fraction within the virial radius of the halo.

^b Specific angular momentum inside R_{vir} .

Stellar particles are color coded according to their age in a rainbow scale, with the reddest particles being oldest. Ages range between about 6 Myr to 5.5 Gyr ($z = 1.0$) and 12 Myr to 8.7 Gyr ($z = 0.43$). Unlike run D4, in which a young stellar disk embedded in an older thick disk can be appreciated, the young stellar population of run R2 at $z = 1.0$ is distributed in a “puffy” spheroidal structure. At $z = 0.43$, 3.2 Gyr since $z = 1$, the once young stellar disk of run D4 has aged, while in run R2 a young stellar disk has formed. This illustrates the large effects the SF/feedback prescription has on the structure of the analyzed galaxies (see also, for example, Scannapieco et al. 2008).

In column (5) of Table 3, we report, for $z = 1.0$ and 0.43, the galaxy stellar effective radius, R_e , defined as the radius where half of the central galaxy stellar mass M_* (disk and spheroidal components) is contained. We find that the galaxy stellar structure is systematically larger as n_{SF} decreases (sequences D1 \rightarrow D2 for the deterministic model, and R4 \rightarrow R3 \rightarrow R2 for the random model). This radius is particularly small for those runs where feedback is inefficient, D1 and D2; when the radiative cooling is artificially switched off allowing for thermal pressure-driven feedback, the radius increases by a factor of ~ 2 (from run D2 to D3). However, R_e seems to be insensitive to the stellar particle mass distribution (compare runs D3 and D4).

Figure 3 show the stellar surface density profiles along the disk plane, averaged azimuthally in concentric cylindrical rings, for all the runs at $z = 0.43$; radii are normalized to their corresponding R_e . In most cases, the surface density profiles can be described approximately by two exponential laws: an inner nearly exponential profile associated to a disk+bulge system and a more extended outer exponential profile associated to an older spheroidal structure (stellar halo). It is interesting that the outer profiles of the R models tend to be higher and more extended than those of the D models. This is probably because models with a stochastic SF scheme favors star formation in low gas density environments, helping the formation of an exponential stellar halo.

The measured effective stellar surface densities of the various runs, $\Sigma_M = M_*/2\pi R_e^2$, lie in the higher density side but within the range of observational determinations at $z \approx 0.4$ and $z \approx 1$; in other words, the simulated galaxies have smaller R_e for their masses than the average radii inferred from observations (see e.g., Barden et al. 2005).

In order to quantify the relative contribution of the spheroidal and disk components to the total galaxy stellar mass we compute the ratio, ϵ , between the z component of the angular momentum of the stellar particle and the angular momentum expected for a circular orbit,

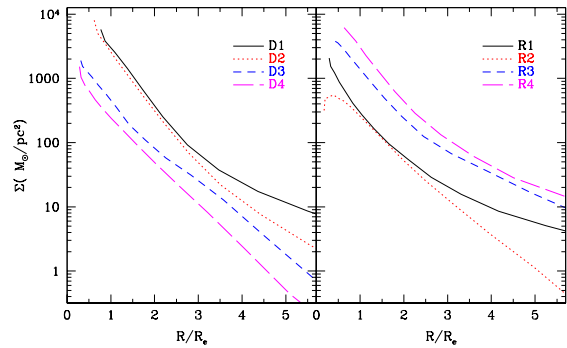


FIG. 3.— Stellar surface density profiles for the D (left panel) and R sequence of runs at $z = 0.43$.

$j_c = RV_c(R)$. We roughly define the mass of the spheroid as twice the mass of all stellar particles with $\epsilon < 0$. The mass of the stellar disk is then estimated as the difference between the stellar mass reported in Table 3 and the mass of the spheroid. In all runs, the spheroidal stellar component is significant (between $\sim 30\%$ and $\sim 60\%$ of M_* at $z = 0.43$) and with old/intermediate ages. The runs with the best defined stellar disks are R1, D3, and R3. The spheroid-to-total stellar mass ratio for these runs is $\approx 30 - 35\%$; the complement is roughly the disk component. It should be mentioned that run R1 follows a model constructed to reproduce Milky-Way-sized galaxies (Ceverino & Klypin 2009).

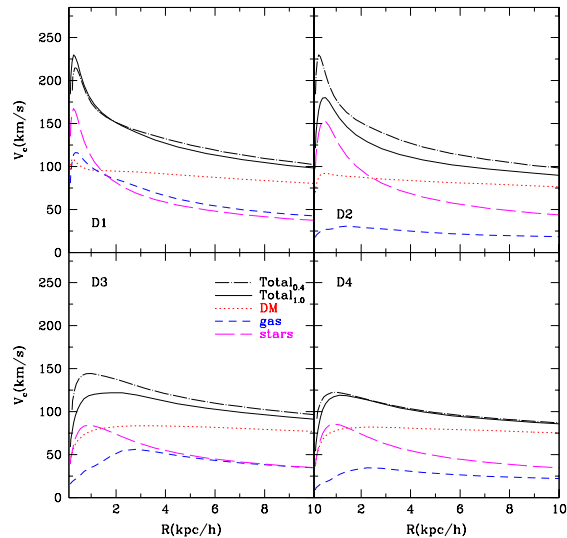


FIG. 4.— Circular velocity profile decompositions for the D sequence of runs at $z = 1$: gas (short-dashed line), dark matter (dotted line), stars (long-dashed line), and total (solid line). Only the total profiles are shown also for the epoch $z = 0.43$ (thick dot-dashed line). Runs in which cooling is always on, D1 and D2, show very peaked profiles, being run D1 the most extreme. On the other hand, run D3 and specially run D4, show relatively flat profiles.

3.2. Circular velocity decomposition

Figures 4 and 5 show the total circular velocity profiles for the R and D models described in Table 1 at $z = 1.0$ (solid line) and 0.43 (dot-dashed line). The circular velocity is defined as $V_c = \sqrt{GM(R)/R}$, where $M(R)$ is the total mass, or the mass of a certain galaxy component (dark matter, gas or stars), contained within radius

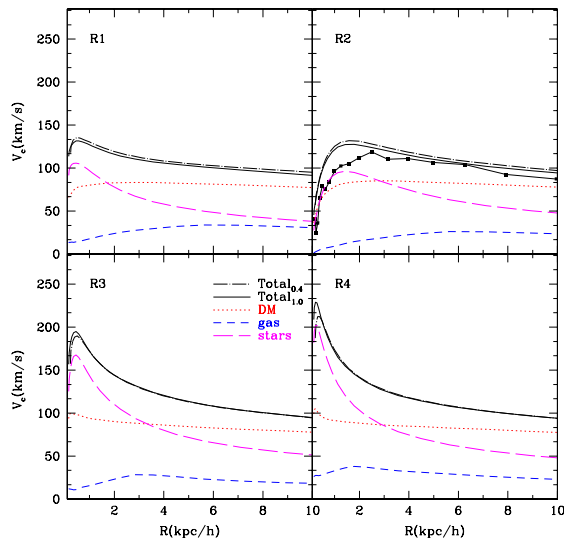


FIG. 5.— As in Figure 4 but for the R sequence of runs. Here we have also added the rotational velocity of the cold gas ($T < 10^4$ K) that is inside the disk and plotted with a solid line with symbols (squares). Runs R2, R3, and R4 differ only in the value of n_{SF} and it increases as we go from R2 to R4. A clear trend of increasing V_c and steepening of the profile is seen. Runs R2 and R1 have a relatively flat circular velocity profile.

R. The circular velocities due to the various mass components are plotted only for epoch $z = 1.0$.

In both, the deterministic ($D2 \rightarrow D1$) and the stochastic (random) runs ($R2 \rightarrow R3 \rightarrow R4$), we see that an increase in n_{SF} translates into more centrally concentrated stellar and gas structures, which produces a more peaked total circular velocity profile. The halo also becomes more concentrated, but this is a consequence of the baryonic gravitational drag. As expected, for our spatial resolution, the contribution of the gas component to V_c increases as n_{SF} increases. This trend might change if tens of parsec resolution is reached. The lack of efficient feedback produces stellar disks that are too concentrated (runs D1 and D2); when local cooling is switched off temporarily, keeping all other parameters fixed, $V_c(R)$ flattens significantly (run D2 to D3).

It is interesting to note that run R2 has a mild declining circular velocity curve. However, this run has no disk at $z = 1$, as seen in Figure 2. Nevertheless, a disk forms later on and its V_c becomes slightly more peaked. Runs D3 and D4 also have mild circular velocity curves at $z = 1$, but, unlike run R2, these runs do have well defined young stellar disks at this redshift. As time goes on, the circular velocities of these models become more peaked and the galaxies more concentrated (see Figure 4). Interestingly enough, such an evolution is much less pronounced for runs with the random SF prescription (see Figure 5).

Lastly, it is important to say that the average rotational velocity in the mid-plane of the disk does not trace the galaxy circular velocity in our simulated galaxies (see, for example, Figure 5). In some of our models, the tangential velocity profile slowly increases with radius as it is observed in low-mass galaxies (e.g., Persic et al. 1996, but see Swaters et al. 2009). Notice, however, that at the current resolution our galaxies do not present a central bar. Similar situations in which rotation curves do not trace the circular velocity have been discussed

by Valenzuela et al. (2007) and Rhee et al. (2004). In these cases the difference is attributed to pressure gradients and non-circular motions.

3.3. Star formation history

Figure 6 shows the SF history (SFH) for the various runs, defined as the instantaneous SFR as a function of time, and computed for each run using the last snapshot recorded. Specifically, in each data dump, in addition to the positions and velocities for all stellar particles, we also save the time at which they formed, their masses (initial and present), and metallicities due to supernovae of types Ia and II. We add up the (initial) masses of the stellar particles formed during a certain time interval, which we take as 0.1 Gyr, and divide it by this time, to obtain the “instantaneous” SFR. Since the amount of stellar mass outside the galaxy is small during the epochs analyzed ($< 3\%$), the SFH computed inside R_{vir} is basically that of the galaxy. The simulations were run until $z = 0.43$, which corresponds for the cosmology used here to a cosmic age of 8.9 Gyr.

In all runs, the SFHs are characterized by a fast increase lasting in most cases 1.5–2.0 Gyr followed by a nearly exponential decreasing phase. Runs with smaller values of n_{SF} show a more gradual decrease in general and the peak of the SFH is shifted to later epochs (sequences $R4 \rightarrow R3 \rightarrow R2$, and $D1 \rightarrow D2$). In the case of the R sequence, the increasing phase is also more gradual and the amplitude of the maximum decreases with decreasing n_{SF} . Run R2, which has $n_{\text{SF}} = 0.1 \text{ cm}^{-3}$, exhibits the most gradual SFH initial increase and the latest SFH maximum ($t \sim 3.5\text{--}4$ Gyr). Runs R3 and R4 are those with the fastest SFR decline with time.

The SFH is also strongly affected by the stellar ability to heat the surrounding gas. The amplitude of the initial maximum in run D3, in which the cooling is temporarily switched off, is lower, and its subsequent decrease is more gradual, as compared with run D2. The SFH of the former run is much burstier than the one of the latter run, with periods of very low SF activity followed by intense bursts. This bursty behaviour is even more pronounced in run D4, a run similar to D3 but with more massive stellar particles (compare also the SFHs of runs D1 and D2). Notice also that in general runs with the random SF prescription tend to have a less bursty SFH than those with the deterministic one.

3.3.1. Relationship between star formation rate and gas density

Figure 7 shows the average SF rate (SFR) surface density, Σ_{SFR} , versus the gas surface density, Σ_g , for all the runs at $z = 1$ and $z = 0.43$. The surface SFRs are computed using the surface densities of stellar particles with ages smaller than $4.0 \times 10^7 \text{ yr}$. For the gas surface density, only gas with $T_g < 10^4 \text{ K}$ is considered. Cylindrically-averaged values of both quantities with a constant radial bin of $0.5R_e$ wide and $0.5 h^{-1} \text{ kpc}$ proper height are obtained for each model and each epoch. For each run, a number of points are plotted with this number depending on the extent of the simulated galaxy. The symbols corresponding to each run are given in the figure caption. The symbols connected by the dotted and solid lines correspond to $z = 1.0$ and $z = 0.43$, respectively. The large symbols correspond to averages of Σ_{SFR} and Σ_g inside

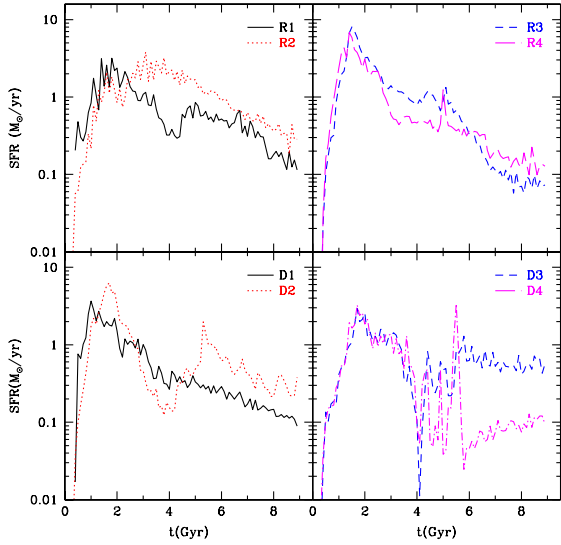


FIG. 6.— SFR histories for all runs presented in this paper. Each panel shows two runs labeled inside panels. In the X axis runs the cosmic time. The last time shown corresponds to $z = 0.43$. For given run, the SFR as a function of time is computed using the snapshot at $z = 0.43$ by tracing back the recorded formation times and initial masses of the stellar particles that are inside the virial radius.

$3R_e$. Notice that surface gas densities move to the right (left) if we take a longer (shorter) cylinder.

As expected, as we go to smaller n_{SF} values (sequences $R4 \rightarrow R3 \rightarrow R2$, and $D1 \rightarrow D2$), the points move down and to the left side of the $\Sigma_{SFR}-\Sigma_g$ diagram. Stellar feedback (see for example, from run D2 to run D3), does not impact significantly the $\Sigma_{SFR}-\Sigma_g$ diagram; at $z = 0.43$ these runs occupy a similar locus in this diagram. As time goes on, while Σ_g decreases slightly, Σ_{SFR} decreases strongly for most of the cases. In general, for a given simulation, the correlation of Σ_{SFR} with Σ_g , both along the radius and at two epochs, is steep and becomes steeper as Σ_g decreases.

3.4. Properties of the interstellar medium

3.4.1. Probability density functions (PDFs)

Figures 8 and 9 show the normalized probability density function, PDF, of gas number density for the D and R series, respectively. Thin solid and dotted lines refer to measurements at $z = 1$. The latter show the PDFs computed using all cells in the maximum level of refinement, $l = l_{max}$, while the former represent the PDFs computed using the cells contained within a cylinder with a radius of $3R_e$ and height of $0.6 h^{-1}$ kpc proper, centered on and oriented with the disk. The normalization volume, V_{tot} , differs in both cases, being smaller for the cylinder. The thick dot-dashed line refers to the PDF measured for the gas within the cylinder at $z = 0.43$. The plane of the disk is defined as the plane normal to the angular momentum vector of the cold gas located in an inner cylindrical shell of radii of 0.5 and $3 h^{-1}$ kpc comoving. We have varied the inner and outer radii of the cylinder and found negligible variations in the measured quantities. Notice that PDFs computed using the cells at $l = l_{max}$ include a significant fraction of cells that contain low-density warm and hot gas. This is due to the fact that these low-density gas cells are kept refined because the dark matter density cell refinement criterium is satisfied.

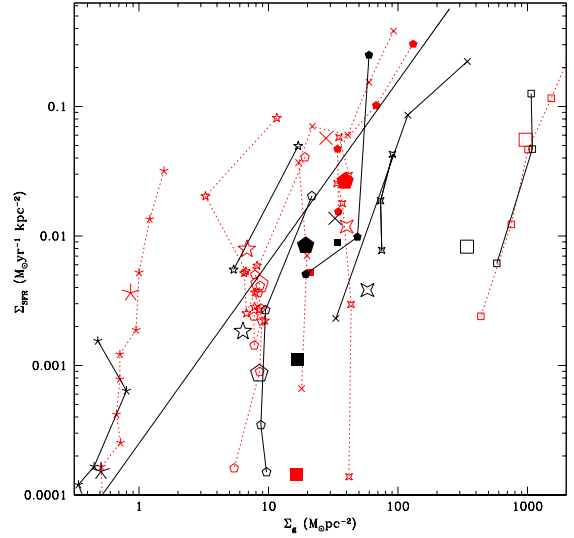


FIG. 7.— Radial SFR surface densities, Σ_{SFR} , versus radial gas surface densities, Σ_g , for each one of the runs at two epochs. The points of a given run are plotted with the same symbol and connected with (red) dotted lines for the epoch $z = 1.0$ and with solid (black) lines for $z = 0.43$. The large symbols show the corresponding average value of Σ_{SFR} and Σ_g of each run at the two epochs (see the text for more details on how the radial and average Σ_{SFR} and Σ_g were calculated). The symbol code for each run is as follows: D1 (open square), D2 (skeletal, four-end), D3 (open star, four-end), D4 (solid square), R1 (open pentagon), R2 (skeletal, five-end), R3 (open star, five-end), and R4 (solid pentagon). The solid line is the fit to observations by Kennicutt (1998).

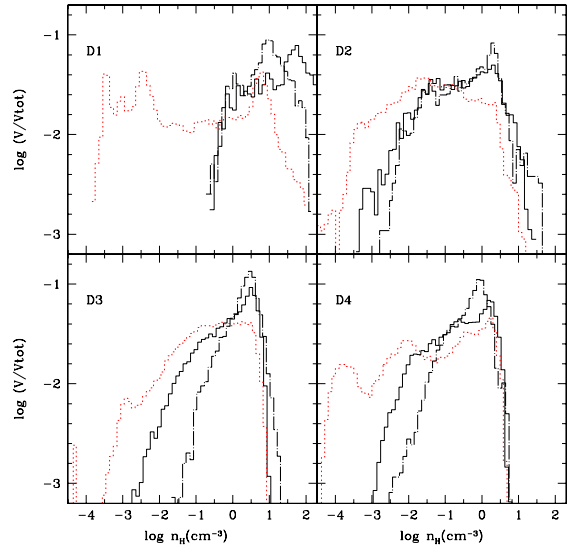


FIG. 8.— Probability distribution functions of gas density, n_H , for the runs from series D. The n_H PDF's, the fraction of total volumen occupied by gas in a given density logarithmic bin, were computed at $z = 1$ or 0.43 using all cells in the maximum level of refinement (dotted lines) or using the cells contained in a cylinder of radius $3R_e$ and height $0.6 h^{-1}$ kpc proper (solid and thick dot-dashed lines) centered on the disk. At $z = 0.43$ only the PDFs within the cylinder (thick dot-dashed lines) are shown in the figure to avoid line crowding. The PDF's computed using the maximum level of refinement cover a bigger volume including a greater normalized fraction of low-density gas.

Figures 10 and 11 show the corresponding PDFs of the gas temperature; the line code is as in Figures 8 and 9. As was already noticed, the volume occupied by the cylinder is smaller than that of the cells at the maximum level of

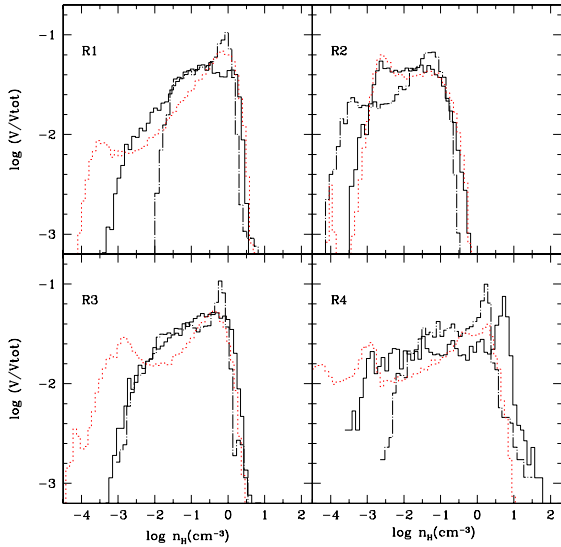


FIG. 9.— As in Figure 8 but for the models of the series R.

refinement. In particular, the temperature PDF of run D1 computed over the cylinder at $z = 1$ contains only cells with $T < 10^4$ K (see upper-left panel of Figure 10); that is, the PDF of this model is only sampling the well-defined cold gaseous disk. Instead, the PDFs computed using the cells at $l = l_{\max}$ contain a significant fraction of warm-hot/hot gas.

Figures 8–11 show that at $z = 1.0$ (the situation is similar at $z = 0.43$, albeit more extreme) all models except R2 have very different PDF's when calculated over the cylinder around the mid-plane than when computed using the grid cells at $l = l_{\max}$. The main difference is the relative absence of hot, low-density gas in the mid-plane: this gas occupies a very small fraction of the disk volume. In particular, we see that in runs D3 and D4, the maximum temperatures in the disk are $T \sim 10^{5.5-6}$ K. On the other hand, we see that the temperature PDF of the finest grid of run D4, in particular, contains a large amount of hot gas, and that its distribution reaches temperatures of up to 10^7 K. This suggests that the hot gas produced by stellar feedback in the disk of run D4 becomes buoyant and leaves the disk. Indeed, run D4 even exhibits a wind (cf. §3.4.2).

Run R2 is the only one at $z = 1$ for which the density and temperature PDF's are very similar when measured for the mid-plane cylinder and for the finest grid. This can be understood because the galaxy in this run has a more spheroidal shape at this redshift. However, at $z = 0.43$ (thick dot-dashed line) a thick disk is already in place (see Figure 2) and the PDF's measured for the mid-plane cylinder and for the finest grid start to deviate from each other, with the low-density hot disk gas buoyantly escaping to the halo.

Let us analyze the PDFs calculated over the cylinder around the rotating mid-plane. We see that as n_{SF} is made smaller (sequences R4 \rightarrow R3 \rightarrow R2, and D1 \rightarrow D2), the density and temperature PDFs become broader. The main effect of the broadening is in the direction of increasing the amount of low-density and warm-hot/hot gas. In the extreme case of model R2, at $z = 1$ a second peak appears in the low-density and high-temperature sides of the corresponding PDFs (see Figures 9 and 11).

The maximum gas density reached by a run also depends on the value of n_{SF} : the lower n_{SF} , the lower the maximum n_{H} value.

Run D2, in comparison to D3 (Figures 8 and 10), shows a higher fraction of low-density, hot gas in both the cylinder or in the highest-refined grid cells (dotted lines). We see here that a stronger feedback (run D3) produces a less dominant hot gas phase, very likely because part of this hot gas is expelled from the mid-plane of the disk. In any case, the galaxy in run D2 is too compact (see Table 3) and shows a rather thick young stellar disk, with its gaseous structure resembling that of run R2. The region in which we compute the PDFs contains a mixture of cold and warm-hot/hot gas, heated very likely by shocks.

From run D4 to run D3 (Figures 8 and 10), the PDFs of density and temperature both within the disk at $z = 1$ (thin solid lines) and in the cells at the maximum refinement level (dotted lines) show a decrease in the lower density and higher temperature regimes. Therefore, by allowing for more massive stellar particles (a more efficient conversion of gas to stars), the galaxy produces a higher fraction of low-density and hot gas.

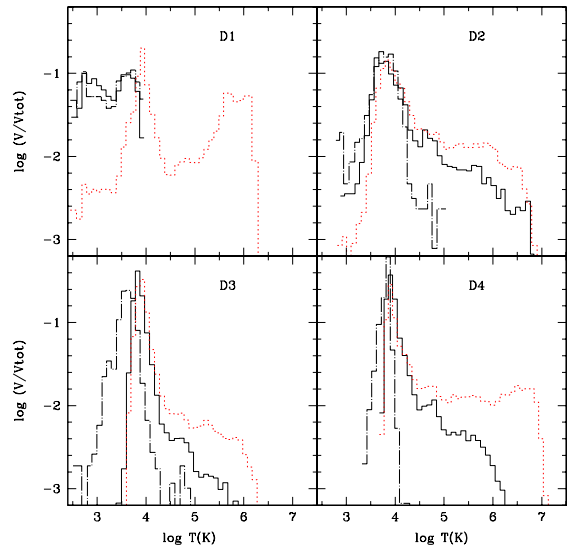


FIG. 10.— Probability distribution function of gas temperature, T , for the runs from series D. The PDF's of temperature, the fraction of total volume occupied by gas in a given temperature logarithmic bin, were computed as explained in the text and in Figure 8. The same line code as in Figure 8 is used here.

3.4.2. Vertical filling-factor profiles

The spatial distribution of the gas in the runs can also be analysed through the filling factors of the gas at various temperature ranges. The vertical profiles at $z = 1$ are shown in Figures 12 and 13. We compute the filling factor over cylinders that have the same radius as the one we use to compute the PDFs; i.e., $3R_e$ of the corresponding simulated galaxy. We define four regimes according to the (azimuthally averaged) gas temperature: cold gas ($T < 3000$ K, *solid lines*), warm gas ($3000 \leq T(\text{K}) < 10^4$, *dotted lines*), warm-hot gas ($10^4 \leq T(\text{K}) < 10^{5.5}$, *short-dashed lines*), and hot gas ($T \geq 10^{5.5}$ K, *long-dashed lines*).

Figures 12 and 13 show that as n_{SF} decreases (sequences R4 \rightarrow R3 \rightarrow R2, and D1 \rightarrow D2) and/or $m_{*,\text{lim}}$

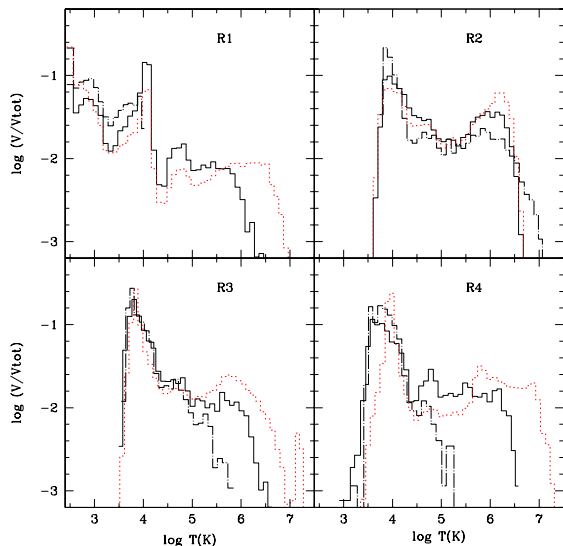


FIG. 11.— As in Figure 10 but for runs of series R.

increases (sequence D1 \rightarrow D2) the fraction of colder gas in the mid-plane decreases and the fraction of hotter gas increases. From these two figures the following other features can also be highlighted: (a) the filling factors of the different gas components change strongly with the height above and below the mid-plane, $|z_d|$. Typically, the fraction of colder gas decreases and that of the hotter gas increases with $|z_d|$; (b) run R2 is the only one where these filling factors remain nearly constant with $|z_d|$, and it is also the only case that presents a non-negligible fraction of hot gas at low disk heights; (c) the ISM in the disk mid-plane of run D1 is composed only of the cold phase; (d) a multiphase ISM with a non-negligible fraction of cold gas at low heights exists only for run R1.

As can be seen in Figs. 12 and 13, the only two runs that presents cold gas in the mid-plane are run D1 and R1. The mid-plane of run D1 is dominated by cold gas because it has a high n_{SF} value, a low stellar mass limit $m_{*,\text{lim}}$, and an inefficient stellar feedback. Run R1, on the other hand, has a significant amount of cold gas in the mid-plane because in this run the UV background ionizing radiation was artificially reduced³ from $z = 8$ to present-day to its value at $z = 8$ and also because it has the largest β , implying that some of the cold dense gas does not form stars, and therefore can remain as such.

In Figure 14 we plot the vertical filling factor profiles of runs D3, D4, R2, and R3 at $z = 0.43$ in order to see how much these profiles could change with time. These are the cases that change most from $z = 1$ to $z = 0.43$. The general trend is that the fraction of colder gas increases in the mid-plane with time (specially in run R3), while the hotter gas ‘moves’ to higher vertical distances. In most of the runs, one observes that with time the warm gas fraction accumulates in a narrow extraplanar layer at $\sim 0.4 - 0.8$ kpc that coexists with the hot gas. At larger heights, the fraction of hot gas already dominates. Run

³ The formula for the ionizing flux, which is based on Haardt & Madau (1996), is taken from Kravtsov (1999). For reference, we note that the fluxes at redshifts $z = 8$, z_{max} , and 1.0 are 5.9×10^{-26} , 7.2×10^{-22} , and 8.5×10^{-23} $\text{erg s}^{-1} \text{cm}^{-2} \text{Hz}^{-1}$, respectively, where z_{max} denotes the redshift at which the ionizing flux is maximum.

D3 at $z = 0.43$ has at the mid-plane $\sim 20\%$ and $\sim 80\%$ of the volume occupied by cold and warm gas, respectively, while in run D4, $\sim 100\%$ is occupied by warm gas. The filling factor of the warm-hot gas in both runs peaks at a height ~ 700 pc, at $\sim 75\%$ and $\sim 90\%$, respectively. The hot gas becomes the dominant component at a height ~ 1 kpc. For the runs R3 and R2, the warm-hot gas is present in the mid-plane, with volume fractions of $\sim 20\%$ and $\sim 40\%$, respectively.

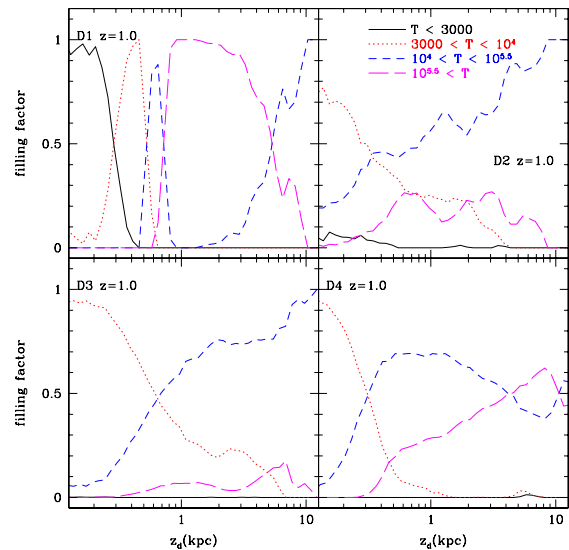


FIG. 12.— Fraction of volume filled with gas at different temperatures as a function of height (below and above the disk plane) for runs of series D at $z = 1$. All runs of the series D present no hot phase in the mid-plane of the disk ($|z| < 300$ pc/h) while runs from D2 to D4 practically have no cold gas ($T < 3000$ K). On the other hand, run D4 is the only D model that has a fraction of hot gas that increases as we go away from the mid-plane of the disk.

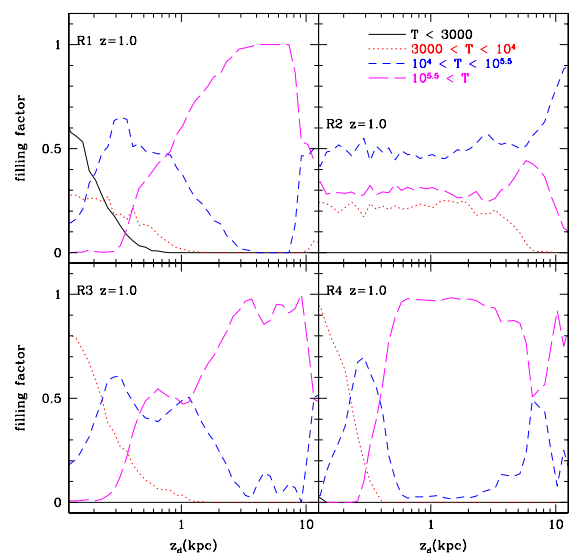


FIG. 13.— As in Figure 12 but for runs of series R. As it was the case for runs D2 to D4, runs R2 to R4 have practically no cold gas whereas, as it happens with run D4, here runs R1 and R3 have a fraction of hot gas that increases as we go away from the mid-plane of the disk. On the other hand, run R2 is the only one in which we found a non-negligible fraction of hot gas in the mid-plane of the disk.

TABLE 3
GLOBAL PROPERTIES OF MODELS

Model	M_{vir} ($10^{10} M_{\odot}$)	M_* ($10^{10} M_{\odot}$)	f_g ^a	R_e ^b (kpc)	$f_{\text{gal}}(R_{\text{vir}})$ ^c	$f_{\text{gal}}(5R_e)$ ^d	J/M(halo) (km s^{-1} kpc)	J/M(baryons) (km s^{-1} kpc)
$z = 1$								
D1	4.69	0.312	0.412	0.24	0.16	0.10	96.0	88.3
D2	4.69	0.466	0.070	0.49	0.12	0.10	203.9	59.9
D3	4.87	0.308	0.446	1.16	0.13	0.11	208.8	287.1
D4	4.87	0.304	0.210	1.17	0.10	0.08	195.9	143.3
R1	4.79	0.332	0.133	0.90	0.13	0.07	188.1	118.6
R2	4.99	0.579	0.076	1.46	0.14	0.11	205.2	107.6
R3	4.81	0.625	0.043	0.64	0.15	0.12	218.9	90.5
R4	4.80	0.524	0.065	0.37	0.15	0.10	232.0	51.3
$z = 0.43$								
D1	5.40	0.358	0.396	0.41	0.17	0.10	143.9	119.5
D2	5.54	0.546	0.060	0.51	0.13	0.10	218.1	57.9
D3	5.84	0.429	0.369	1.00	0.13	0.11	199.6	261.3
D4	6.60	0.309	0.229	1.11	0.09	0.06	49.4	149.7
R1	5.64	0.379	0.161	1.08	0.13	0.07	240.8	159.1
R2	6.21	0.676	0.075	1.80	0.13	0.11	141.2	167.8
R3	5.49	0.640	0.043	0.73	0.13	0.11	203.7	93.8
R4	5.63	0.571	0.051	0.50	0.13	0.10	229.4	49.9

^a Gas fraction as defined by $f_g \equiv M_{\text{gas}}/(M_{\text{gas}} + M_*)$, where only gas cells with $T_g < 10^4$ K are used.

^b Effective radius defined as the radius where half of the central galaxy stellar mass is contained.

^c Baryon fraction within the virial radius of the halo using all baryons, gas at all temperatures plus stars.

^d Baryon fraction within five effective radius using only stars plus gas with $T_g < 10^4$ K.

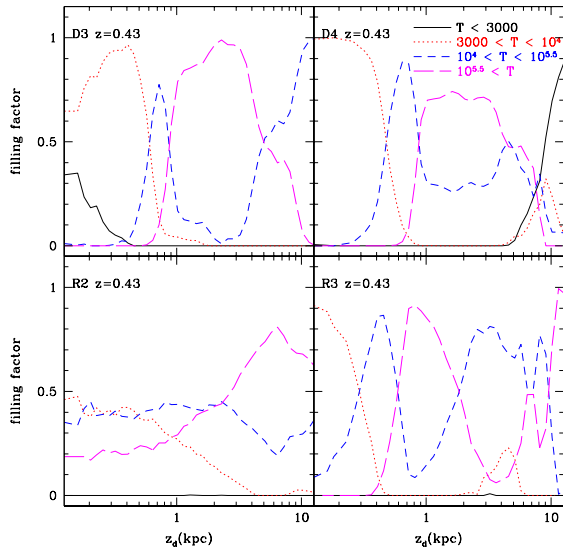


FIG. 14.— Fraction of volume filled with gas at different temperatures as a function of height (below and above the disk plane) for runs D3, D4, R2, and R3 at $z = 0.43$. These are the runs that most change their vertical filling factors since $z = 1$.

3.5. The mass and angular momentum fractions

In Table 3, M_* and the gas fraction, f_g , of the galaxies in the different runs are reported for $z = 1$ and 0.43. The gas fraction is defined as $f_g \equiv M_{\text{gas}}/(M_{\text{gas}} + M_*)$, where only gas cells with $T < 10^4$ K are used for the gas. The stellar and gas masses were measured within a sphere of radius $5R_e$. We see that for runs without efficient feedback, runs D1 and D2, f_g strongly decreases (gas is consumed efficiently) as n_{SF} diminishes and, to a lesser degree, as $m_{*,\text{lim}}$ increases. Runs with a stochastic SF scheme do not show a clear trend of f_g with n_{SF} . From run R4 to R2, f_g first decreases (runs R4 \rightarrow R3) and then it increases (runs R3 \rightarrow R2). On the other hand, run R1 is the run, within the R series of runs, with highest f_g

fraction at both $z = 1$ and 0.43.

The shape of stellar particle mass distribution seems to influence the value of f_g : for cases where this distribution extends to high-mass stellar particles, f_g is smaller (from run D3 to D4 and partially from run D1 to D2). Note that in run D4 the feedback is so strong that a galactic wind is produced and as a result a significant fraction of gas is ejected from the disk. Finally, from Table 3 it is inferred that runs with the random SF scheme are more efficient in transforming gas into stars than those with the deterministic scheme (the f_g values of R runs are systematically smaller than those of runs D). However, it should be noted that as a consequence of the low value of C_* and the SF scheme, gas is transformed locally into stars less efficiently in runs D1 to D3 than in the R runs.

Columns (6) and (7) of Table 3 show the mass baryon fraction using all baryons (gas at all temperatures + stars) within R_{vir} , and using only those baryons (gas with $T_g < 10^4$ K + stars) within a sphere of $5R_e$ around the galaxy center, respectively. The latter case is related to what is called usually the galaxy baryon fraction. Several kind of estimates and observational inferences show that this fraction in present-day galaxies is much smaller than the universal value, equal to 0.15 for the cosmology used here. A radius of up to $5R_e$ was used to compute f_{gal} to encompass the gaseous disk, which is typically larger than the stellar disk.

The galaxy mass baryon fraction, $f_{\text{gal}}(5R_e)$, does not depend on the value of n_{SF} , as is seen from the runs where this parameter is changed systematically, (sequences R4 \rightarrow R3 \rightarrow R2 and D1 \rightarrow D2). From run D2 to D3, $f_{\text{gal}}(5R_e)$ is almost the same, showing that switching off local cooling by 40 Myr, at least in this simulation, does not produce a net loss of baryons from the galaxy. However, from run D3 to D4, both the halo and galaxy baryon fractions decrease significantly. At $z = 0.43$ run D4 has the lowest values of these fractions among all the runs. Therefore, a bias toward massive particles m_* dis-

tribution along with efficient feedback induces strong gas ejection from the galaxy and halo.

According to Table 3, the fraction of baryons within the halo but outside the galaxy is non-negligible for all the runs. The extreme cases are runs D1, R1 and R4 where 50% or more of the baryonic content of the corresponding halo is outside the central galaxy. These baryons are in the form of shock-heated gas or gas heated and expelled from the central galaxy; a small fraction is in stars in satellite galaxies. The halo with the smallest baryon fraction corresponds to run D4 at $z = 0.43$, with $\sim 60\%$ of the universal fraction. This run is the one with the most efficient galaxy outflows.

Columns (8) and (9) of Table 3 present the total specific angular momentum (AM) for the dark matter halo and for the sum of the stellar and cold gas components of the central galaxy (within a sphere of $5R_e$ radius), respectively. The specific AM is given in units of $\text{km s}^{-1} \text{kpc}$. The total specific AM measured at a given time is sensitive to the current halo and galaxy assembly events, nevertheless, with a couple of exceptions, values are around $200 \text{ km s}^{-1} \text{kpc}$, a value similar to those found in the adiabatic run (see Table 2). In this latter case the halo is almost not ‘perturbed’ by the baryonic processes. We found that the specific AM of the DM halo is typically, as expected, greater than the corresponding specific AM of the baryonic component. The effects of complex baryonic processes in the different runs produce variations in the halo mass assembly history as well as in the properties of the surviving subhalos. Such variations are on the basis of the different values of the halo’s specific AM measured in our different runs, at epochs where the halo is yet in a relatively active phase of mass aggregation.

In spite of the transient nature of the specific AM measures mentioned above, some general results can be highlighted. We see, as expected, that in most of the runs the halo’s specific AM is larger than the galaxy’s specific AM. Nevertheless, the galaxy’s specific AM for those runs with strong feedback is relatively large and in some cases it is even larger than the corresponding halo’s specific AM (see Table 3 run D3). The specific AM in most of the runs remains roughly constant or slightly increases from $z = 1$ to $z = 0.43$. The effect of feedback is clearly in the direction of producing galaxies with larger specific AM (see the change from run D2 to D3). We also see that the galaxy’s specific AM increases as n_{SF} decreases (sequence R4 \rightarrow R3 \rightarrow R2), but this seems to be related to strength of the feedback, it is stronger in low gas density.

4. DISCUSSION

4.1. General trends and SF/ISM properties

In the sequences of runs D2 \rightarrow D1 (deterministic SF model with weak feedback) and R2 \rightarrow R3 \rightarrow R4, (random SF model with efficient feedback) the SF density threshold n_{SF} is increased, keeping the other parameters similar. Our simulations show that as n_{SF} is increased, the overall stellar galaxy has a smaller effective radius R_e and the circular velocity profile is more peaked. For lower values of n_{SF} , the peak in the SFH tends to be slightly shifted to later epochs and the later (nearly exponential) decline in SFR is more gradual. Related to this trend, at smaller n_{SF} , the stellar populations become younger on average, the stellar structure becomes thicker (see also

Saitoh et al. 2008), and a larger fraction of stars exists in a ‘‘puffier’’, more spheroidal component.

Regarding the ISM properties of the simulated galaxies, their PDFs of the density and temperature evolve to broader distributions, with more gas in the low-density, and high-temperature regime in the disk, and a smaller maximum value for the gas density, as n_{SF} is smaller. The gas filling factors above and below the mid-plane also show that for smaller n_{SF} , the cold gas close to the mid-plane become less abundant. We note that in general is not easy to produce cold, high-density gas in the simulations. At $z = 1.0$, only the run with the highest n_{SF} ($= 50 \text{ cm}^{-3}$) and weak feedback (run D1) shows a significant amount of this gas in the mid-plane. At $z = 0.43$, cold and high-density gas is also present in the mid-plane of run D3. On the other hand, a hot gas phase in the disk mid-plane can only apparently be produced by lowering n_{SF} .

It is not clear what a realistic value for n_{SF} should be, but we argued in §2.2 that for a cell of 150 pc, close to the 218 pc of our nominal resolution at $z = 0$, this value should be around 5 cm^{-3} . Moreover, the results of our experiments seem to support this number: a value much higher than this produces a galaxy that is too compact (see, for example, R2 and R3 versus R4 or D2 versus D1, albeit with weak feedback), while a much lower value produces a system that is closer to being a spheroidal galaxy, with a very small fraction of gas, rather than a disk (see Table 3). However, a small value of n_{SF} (0.1 cm^{-3}) may produce reasonable results as shown, for example, by Governato et al. (2007). We speculate that this may be an effect of the different technique (AMR versus SPH) and subgrid physics (feedback) used to simulate galaxy formation.

Saitoh et al. (2008) concluded that values of n_{SF} as high as $\sim 100 \text{ cm}^{-3}$ should be used in high-resolution simulations ($\sim 20 \text{ pc}$) in order to reproduce the complex structure of the gas disk. They also concluded that using high values for n_{SF} makes the model results fairly insensitive to the SF prescription. In our experiments, high values of n_{SF} produce systematically too concentrated galaxies with the hot gas phase being absent from the mid-plane. Yet, results in Saitoh et al. (2008) are actually in agreement with our suggested strategy for choosing n_{SF} on the basis of the gas column density. For a 20-10 pc resolution, our simple argument would indeed suggest values of n_{SF} of 50-100 cm^{-3} .

A second parameter that enters in the SF prescription is the *stellar particle mass limit* $m_{*,\text{lim}}$, defined in §2.2. As was mentioned in that section this is not an absolute lower limit. High values of m_* , for a given cell size, mean that more stellar and SN energy is dumped into the cell. As a result, in models with cooling turned off in the SF regions, the feedback-driven ejection of gas from the disk increases and the SFH of the modeled galaxy becomes more bursty (compare runs D3 and D4). On the other hand, the structural/dynamical properties of the modeled galaxies does not seem to depend strongly on the stellar particle mass distribution.

Regarding the *efficiency of stellar feedback*, we find that it has a strong effect on the structural/dynamical properties of the galaxy as well as on their SFH and ISM properties, in agreement with recent numerical works

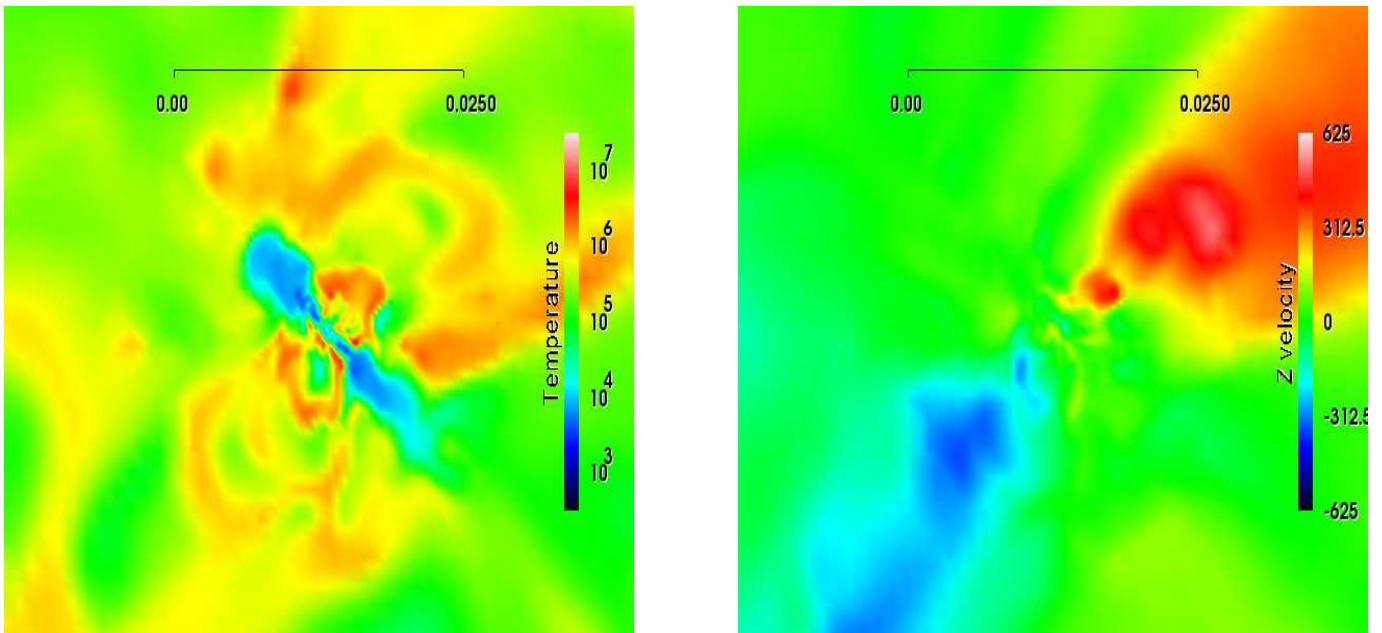


FIG. 15.— Edge-on view of simulation R3 at $z = 1$. *Left panel*: Distribution of the gas temperature. *Right panel*: Distribution of the z velocity component. The slices are 36 comoving kpc on a side (length of solid line) and 219 comoving pc thick. It can be seen that gas velocities can clearly exceed 200 km s^{-1} .

(c.f. Governato et al. 2004, 2007; Scannapieco et al. 2006, 2008; Ceverino & Klypin 2009; Zavala et al. 2008; Dalla Vecchia & Schaye 2008; Stinson et al. 2009). We have experimented by switching off cooling (c.f. Gerritsen & Icke 1997; Thacker & Couchman 2000; Stinson et al. 2006) by 40 Myr in order to allow for proper expansion of the heated regions. This time is roughly the time a pressure-driven super-shell will attain $\gtrsim 150 \text{ pc}$ size and the time a star of eight solar masses live. When this feedback is allowed in our low-mass galaxy, the stellar effective radius increases by a factor of ~ 2 , the galaxy becomes less concentrated, and its $V_c(R)$ profile becomes flatter than in the weak-feedback simulation (c.f. runs D2 and D3). A stronger feedback helps also to keep an episodic SFH. A complex multi-phase structure in the disk is favored by the action of feedback but if it is too strong, the low-density, warm and hot gas can be completely blown away from the disk, as it seems to be the case in run D4.

The warm and hot gas seen above the disk plane can be produced by two mechanisms: (1) shocks of the infalling gas, and/or (2) gas heated and ejected from the mid-plane by supernovae and stellar winds. Which is the dominant process depends on the infalling history of the gas and on the efficacy of the stellar feedback. For example, in run D1 (weak feedback) it is very unlikely that the hot gas seen at intermediate altitudes ($\sim 1-3 \text{ kpc}$) is produced by the second mechanism. On the other hand, the increasing amount of hot gas seen at very high altitudes (as high as $\gtrsim 5 \text{ kpc}$) in runs D4, R3, and R4 at $z = 1$ appears to come from the second mechanism. This is confirmed visually and by the analysis of the gas v_z distribution, where v_z is the gas velocity component perpendicular to the plane of the disk. Figure 15 shows run R3 at $z = 1$. The projected spatial distribution of the gas temperature and of the z velocity component are shown in left and right panels, respectively. Figure 16, on the other hand, shows the v_z normalized distribution

of runs D1, D3, D4, and R3 at $z = 1$. Here we have used all cells inside R_{vir} . Unlike runs D1 and D3, runs D4 and R3 exhibit high $|v_z|$ wings, corresponding to a galactic wind.

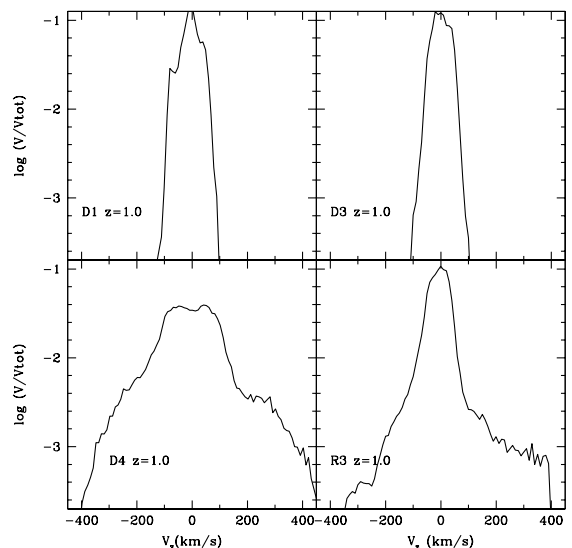


FIG. 16.— Distribution function, weighted by volume, of the vertical velocity component of the gas for the analyzed galaxy at $z = 1$ for runs D1, D3, D4, and R3. We have used all cells within R_{vir} . As was already seen in Fig. 15 runs D4 and R3 exhibit outflow velocities that go up to 400 km s^{-1} .

4.1.1. Self-regulated SF and the multi-phase ISM

Several of the results described above can be understood as a consequence of the efficiency by which the thermal energy is injected into the ISM and the ability of the medium to self-regulate its SF. The R2–R4 random-SF sequence (cooling turned off after SF events) shows that the reduction in n_{SF} causes: (a) a flatter circular

velocity profile; (b) a stronger spheroidal stellar component; (c) a thicker disk; and when run R2 is compared with R3 or R4, (d) a delay of the maximum of SFR. The deterministic-SF sequence shows that, at fixed n_{SF} (runs D2, D3, and D4), a greater ability of SF to heat the gas causes a more efficient self-regulation of SF, preventing the gas from going into stars too rapidly. This gives flatter $V_c(R)$ profile and allows the gas to settle into an extended disk configuration. However, when feedback is strong enough to produce galactic superwinds, the self-regulation can be interrupted and SF proceeds in a bursty regime. Indeed, run D4 is the one where ejecting feedback is most efficient and it is also the one with the most bursty SFH.

A multi-phase structure of the galactic ISM is not easy to attain in cosmological numerical simulations (see for a discussion, e.g., Stinson et al. 2006; Ceverino & Klypin 2009). For example, we see in run D1 that only the cold phase is present in the mid-plane of the disk while in run D2 the hot phase is absent (see Figure 12). These two runs have an inefficient feedback, but even in those for which the cooling is switched off for 40 Myr after each SF event (strong feedback, runs D3 and D4), the hot phase is also absent. The only run in which a multi-phase medium is observed at the analyzed epochs is R2. Its density and temperature PDFs show wide and nearly bimodal distributions, with different gas phases, from cold-warm dense gas to hot low-density gas, coexisting within the galaxy. The increase of the SFR with time of run R2 is more gradual and not too bursty, which suggests a more uniformly self-regulated SF process with only small episodic phases. Finally, this run takes the longest time to assemble the disk.

In summary, the results of our experiments show that a multi-phase ISM in low-mass galaxies is not a straightforward product of feedback and resolution. While the former certainly helps, in low-mass systems it also produces outflows that leave only cold/warm high-density gas in the galaxy and induce a bursty SFH.

Finally, in our simulations the $\Sigma_{\text{SFR}}-\Sigma_g$ relation tends to be significantly steeper than the empirical determinations for normal disk galaxies, which are typically explained by the quiescent, self-regulated nature of the SF process (e.g., Kennicutt 1998; Hernández et al. 2001; Martin & Kennicutt 2001). For reference, we plot in Figure 7 the fit to observations by Kennicutt (1998) for averages values of normal disk galaxies, their centers, and starburst galaxies (solid line). This correlation is roughly maintained for azimuthally averaged elements along a given disk (Martin & Kennicutt 2001). As can be seen, most of our runs at both $z = 1$ and $z = 0.43$ show a steeper local correlation than the observational fit of normal galaxies. Overall, most of the simulation points lie around the observational fit. The points from run D1, which is the run that suffers most from the overcooling problem, are the most distant from the fit. It is interesting to note that among LSB galaxies and along their azimuthally averaged elements, the $\Sigma_{\text{SFR}}-\Sigma_g$ correlation has been found to be significantly steeper than the given by Kennicutt (Wyder et al. 2009). LSB galaxies are typically of low mass.

4.1.2. The simulation with run-away stars (run R1)

The subgrid physics used in run R1 differs from the rest of simulations explored herein. In run R1 the radiative cooling is not switched off but a significant fraction of stars are modeled as runaway stars able to migrate to lower gas density regions. The SN explosions in the lower density gas, where the cooling time is long, are more efficient. This model has been successful in reproducing many of the properties of Milky Way-sized galaxies (Ceverino & Klypin 2009; Ceverino et al. 2009). As shown here, it works reasonably well also for a low-mass galaxy. It successfully reproduces a roughly flat $V_c(R)$ profile and a multiphase ISM at the galaxy mid-plane. The model also has the lowest galaxy mass baryon fraction and relatively high angular momentum content. On the other hand, its SFR was relatively too efficient at early epochs (the first 1-2 Gyr). As a result, at later times, $z < 1$, the SFR was lower than other ‘feedback-efficient’ models, and the model ends up with a lower fraction of mass in gas (see, for example, R1 versus D3). These effects are probably caused by the high value used for the star formation efficiency, C_* . Overall, run R1 exhibits similar properties to those of run D3 and D4 as a result of its ability to heat the gas efficiently through the runaway stars.

4.2. Galaxy assembly in low-mass Λ CDM halos

Our simulations suggest that the effects of feedback are more relevant for the galaxy morphology than in massive systems. The main effects are *galaxy outflows and a trend to form a significant extended stellar spheroid with an approximately exponential surface density profile*. What is the origin of this stellar halo? Since the dark matter halo under study evolves in a quiet fashion, at least from $z \sim 2$ to $z \sim 0.4$, without experimenting major mergers, a significant fraction of the stellar particles of this extended spheroid were born in situ and *not by mergers* as it is expected for large galaxies. This is confirmed by our analysis of tracing back in time the position of the stellar particles in order to infer their origin. Recently, Stinson et al. (2009) have also reported the formation of old extended exponential stellar halos in their simulations of dwarf-like galaxies in isolated (without mergers) halos. As these authors review, observations show that dwarf galaxies are characterized by extended exponential old/intermedium age stellar halos. A recent study of LSB galaxies with the stacked image technique has also shown the existence of red faint stellar halos around LSB galaxies (Bergvall et al. 2009), galaxies that are supposed to form typically in isolated environments. It is worth noticing that the R runs (those with a stochastic SF model), with the exception of R2, produce more massive and extended stellar halos than the D runs (those with deterministic SF model), as seen in Fig. 3.

The parameters of the SF/feedback prescriptions used here were shown to affect significantly the evolution and properties of the modeled low-mass galaxy. The change of these parameters affects in a complex and non-linear way the evolution and properties of the system. We note that even the evolution of the dark matter mass and angular momentum distributions is different for different combinations of the SF/feedback parameters, confirming the existence of a *tight evolutionary interconnection between baryons and dark matter* (see for recent results, e.g., Weinberg et al. 2008; Abadi et al. 2009;

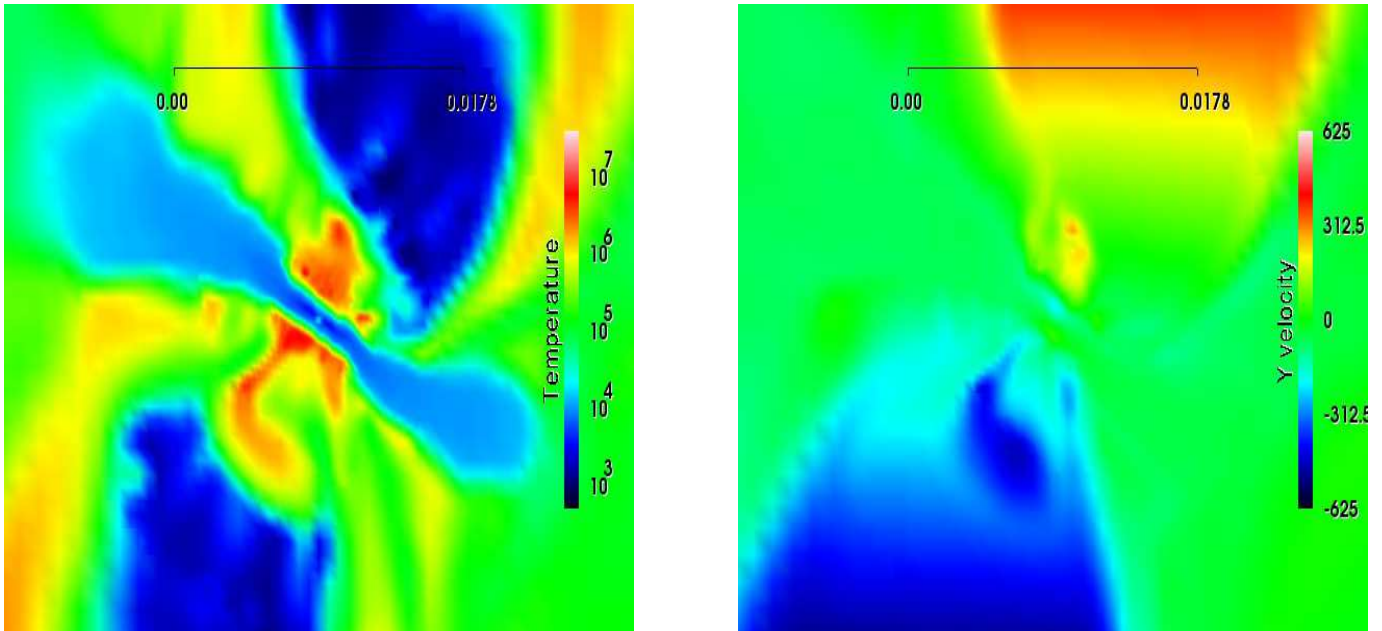


FIG. 17.— Edge-on view of model D4 at $z = 0.43$. *Left panel:* Distribution of the gas temperature. *Right panel:* Distribution of the velocity component perpendicular to the disk. Slices are 25 comoving kpc on a side (length of solid line) and 219 comoving pc thick. It can be seen that the gaseous disk is warped and more homogeneously distributed than that shown in Figure 15. Gas velocities are no longer structured in shells and velocities exceed 300 km s^{-1} far from the disk.

Pedrosa et al. 2009). In particular, the internal distribution of the angular momentum evolves in our simulations, as can be seen, in particular, by changes in the dark halo and baryonic galaxy specific angular momentum ratio. We suggest that our finding that the baryon specific angular momentum can be larger than the one in the dark halo, deserves further future exploration.

In order to obtain a not too concentrated low-mass galaxy, with a nearly flat rotation curve, multi-phase ISM, and an extended and episodic SFH, an efficient stellar feedback is necessary (in our case, switching off radiative cooling in the star forming region by 40 Myrs). However, the SF parameters are also important; for the resolution we have attained in our simulations (nominally 218 comoving pc), effective values for the density threshold $n_{\text{SF}} \sim 1 - 10 \text{ cm}^{-3}$ are recommended. We say ‘effective’ because in the stochastic (random) SF scheme the reported n_{SF} is just the minimum value, larger values of n_{SF} are actually chosen, and SF proceeds with a probability distribution given by eq. (1). As in previous related numerical treatments of the galaxy problem, we conclude that sub-grid physics needs to be carefully addressed (tuned) in order to obtain reasonably realistic galaxy properties.

4.3. Shortcomings

Despite that several of the runs presented here predict realistic properties⁴, we note that the circular velocity curves are decreasing for all the cases studied here, while in observed low-mass galaxies the trend is to have an increasing *rotation curve* up to the last measured radii (c.f. Persic et al. 1996, but see Swaters et al. 2009). However, the average rotational velocity profile does not trace necessarily the circular velocity and at least in model R2

the rotational velocity, of the gas at $T < 10^4 \text{ K}$, increases as observed in low-mass galaxies. Similar situations have been discussed by Valenzuela et al. (2007) as a result of pressure gradients and non-circular motions. The mismatch between circular and rotation velocity deserves further exploration in future papers exploring also effects of resolution.

Also, our simulated galaxies show baryonic mass fractions that are too high compared with observational inferences. For example, in the simulation where galaxy outflows are most effective (run D4), $f_{\text{gal}}(5R_e) = 0.06$ (at $z = 0.43$) is only a factor 2.5 lower than the universal baryon fraction f_b , while the observational inferences suggest that present-day galaxies of low masses have baryon fractions more than a factor of 5 smaller than f_b . Our results confirm that *producing a stellar feedback that is sufficiently efficient as to eject considerable amounts of gas from even low-mass galaxies is not an easy task* (see also Dubois & Teyssier 2008, and references therein).

Even more, the problem of producing strong enough outflows is probably in opposition with other potential vexing conflict. An increasing amount of local and high-redshift observational evidence shows that the less massive the galaxies, the higher their current specific SFRs (SSFR = SFR/M_*) on average at all redshifts back to $z \sim 1-2$, a phenomenon dubbed as ‘downsizing in SSFR’ (Fontanot et al. 2009). Moreover, the observational inferences show that the problem is not that massive disk galaxies have low SSFRs but that low-mass galaxies have too high SSFRs (see for a discussion Firmani et al. 2009, and references therein). Such SSFRs imply that low-mass galaxies should delay the formation of stars and do it with a nearly constant or even increasing SFRs (Noeske et al. 2007). On the other hand, if f_{gal} decreases as the galaxy mass decreases, then obtaining late, high SSFRs in these galaxies becomes even more diffi-

⁴ The aim of the present work was not to produce a realistic galaxy.

cult. As concluded in Firmani et al. (2009, see also Somerville et al. 2008 and Fontanot et al. 2009) both problems are difficult to solve in the context of Λ CDM-based models.

The cosmological numerical simulations presented here confirm the sharpness of both potential problems. *The baryon fractions of the simulated low-mass galaxies are too high and their SSFRs are in all cases much smaller than the average values of the observational inferences at redshifts $\sim 0.4 - 1$.* The run with the highest SSFRs is D3: SSFR = 0.17, 0.06 Gyr⁻¹ at $z = 1$, 0.43, respectively. Observations of large samples of late-type galaxies at high redshifts report values ~ 5 times higher for the corresponding z 's and stellar masses (Bell et al. 2007; Zheng et al. 2007; Noeske et al. 2007; Damen et al. 2009, see also Fig. 1 in Firmani et al. 2009). Most of the other runs have SSFRs much smaller than those of run D3. Our simulations also show that if f_{gal} is reduced by strong feedback-driven outflows, then the late-time SSFR decreases. Run D4 indeed has fewer baryons owing to the strong outflows, but also a much lower SSFR than run D3. A related problem to the low SSFRs is that *the gas fractions of the simulated galaxies (for example at $z = 0.43$) are in most cases too low* (see Table 3). Among runs R2–R4, the maximum value of f_g is 0.075 for run R2; among runs D2–D4, as expected by its SSFR history, run D3 has the largest value, $f_g = 0.37$, which is still marginal compared with the large gas fractions of observed present-day low-mass galaxies. They should have large gas reservoirs to produce the high SSFRs inferred from observations.

If the baryon fraction and SSFR problems for low-mass galaxies are confirmed, models for SF/feedback very different to the one applied here—and in other works—should be proposed to agree with observations, preserving the underlying Λ CDM cosmogony. It is possible that significant changes to the galaxy assembly process can be introduced alternatively by improving the physics of the poorly understood circumgalactic and intergalactic media. Finally, we should say that the current observational inferences, specially at high redshifts, are still plagued by large uncertainties (Conroy et al. 2009a; Conroy et al. 2009b; Firmani et al. 2009).

A comparison of simulation outcomes at $z = 0$ with the more accurate observations of present-day galaxies is desirable in order to assess the severity of the problems mentioned above. We plan to do this in a forthcoming paper.

Finally, it should be mentioned that the sub-grid prescriptions in our simulations are certainly not complete, as several physical ingredients that could be important for the evolution of real galaxies are missing. In particular, our simulations do not include the magnetic field nor cosmic ray pressure, and they do not resolve the whole plethora of phenomena that occur at the scales of molecular clouds, including turbulence and other forms of stellar feedback additional to supernova explosions, such as bipolar outflows and the expansion of HII around massive stars. All of these agents contribute to drive the turbulence at scales that are unresolved in our simulations, whose effect may be to reduce the star formation efficiency in the simulations (Klessen, Heitsch & Mac Low 2000; Vázquez-Semadeni, Ballesteros-Paredes, & Klessen

2003; Mac Low & Klessen 2004; Rosas-Guevara et al. 2010; Vázquez-Semadeni et al. 2010). The magnetic field is expected to have a similar effect (Ostriker et al. 1999; Heitsch et al. 2001; Vázquez-Semadeni et al. 2005). Note that, in a sense, this is what we are accomplishing in our simulations by turning off the local cooling after a star formation event, since the hotter gas is less prone to forming stars. However, future studies will need to quantify these effects so that they can be incorporated in a suitable sub-grid model applicable for galaxy-formation simulations.

5. CONCLUSIONS

By means of high-resolution AMR hydrodynamic simulations (the hydrodynamics + N-body ART code), we have explored the formation and evolution of a galaxy within a low mass halo ($\sim 7 \times 10^{10} h^{-1} M_\odot$ at $z = 0$) assembled in the context of the Λ CDM cosmogony. The DM particle mass of the least massive species is $5.3 \times 10^5 h^{-1} M_\odot$. Our main aim was to explore the formation of a low-mass galaxy in cosmological simulations with *the same initial conditions* but varying the most relevant parameters of the SF and feedback recipes. The analysis presented herein was mainly made at two epochs, $z = 1.0$ and 0.43, a time period of 3.2 Gyr for the used cosmology. From this exploratory study—not exhaustive in any sense—we remark the following systematic results:

- The SF density threshold n_{SF} is a relevant parameter in the simulations, which affects the main structural and dynamical properties of the stellar and gaseous components of the low-mass galaxies, as well as their SFHs and general ISM properties. As n_{SF} is decreased, (a) the stellar galaxy size (R_e) increases; (b) the $V_c(R)$ profile becomes less peaked; (c) the peak in the SFH is delayed and the late (nearly exponential) decline in SFR becomes more gradual; (d) the stellar populations are younger on average, with a thicker disk and a larger fraction of stars in a “puffier”, spheroidal component; (e) the low-density and high-temperature gas in the disk increases. For a cell of 150 pc, close to our nominal resolution at $z = 0$, we estimate from typical ISM properties that n_{SF} should be $\sim 5 \text{ cm}^{-3}$.

- The stellar particle mass limit, $m_{*,lim}$, affects the efficiency of SN energy dumping into the cell. For high values of $m_{*,lim}$, the feedback-driven disk outflows increase and the SFH of the simulated galaxy becomes burstier.

- An effective stellar feedback (generated by turning off locally the cooling by 40 Myr after SF) has a strong effect on our studied low-mass galaxy: the stellar radius R_e increases by a factor of ~ 2 , the galaxy becomes less concentrated, and $V_c(R)$ becomes flatter. A strong feedback produces also an episodic SFH. Its action also favors the development of a complex multi-phase disk ISM and a self-regulated SF process, but if it is too strong, the low-density, warm/hot gas can be completely blown out from the disk.

- For all of our runs, both at $z = 1$ and 0.43, we find that the relation between Σ_{SFR} and Σ_g is steeper than empirical determinations for normal disk galaxies, but in agreement with recent determinations for LSB galaxies, which are typically of low mass. Nevertheless the effective stellar surface densities, Σ_M , of our models are instead in the high-density side of the observed distribu-

tions at $z \approx 0.4$ and 1.

- In all runs, the stellar galaxy has a significant extended spheroidal component (between ~ 30 and 60% of M_* at $z = 0.43$) with a nearly exponential surface density profile. We have seen that an important fraction of the stars in this halo were formed in situ, while a minor fraction may come from minor merger events.

- The variation of the parameters of the SF/feedback prescriptions affects in a complex and non-linear way the evolution of the galaxy system. Even the evolution of the dark mass and angular momentum distributions change as these parameters are changed, confirming the tight interconnection between baryons and dark matter. For example, the internal distribution of AM evolves in our simulations and this evolution is sensitive to the SF/feedback physics.

- In all runs of the low-mass galaxy studied here, the baryon fractions are higher, the gas fractions are lower, and the SSFRs are much smaller than the corresponding average values inferred from observations. In particular,

the too low SSFRs values found in our model galaxies pose a sharp problem to the simulations and the model in general if the yet uncertain observational inferences are confirmed.

ACKNOWLEDGMENTS

We are grateful to A. Kravtsov for providing us with the numerical code and for help with its usage. We are in debt to N. Gnedin for providing us the analysis and graphics package IFRIT. The authors acknowledge PAPIIT-UNAM grants IN112806 to P.C., IN114509 to V.A., and IN118108 to O.V., CONACyT grants 60354 (to P.C., V.A., and O.V) and U47366-F (to E.V.-S.), and the Lady Davis Trust to D.C. for partial funding. We also acknowledge the anonymous referee for a careful reading of the manuscript. Some of the simulations presented in this paper were performed on the HP CP 4000 cluster (Kan-Balam) at DGSCA-UNAM.

REFERENCES

- Abadi, M. G., Navarro, J. F., Steinmetz, M., & Eke, V. R. 2003, *ApJ*, 591, 499
- Abadi, M. G., Navarro, J. F., Fardal, M., Babul, A., & Steinmetz, M. 2009, preprint (astro-ph/0902.2477)
- Avila-Reese, V. 2007, in "Solar, stellar and galactic connections between particle physics and astrophysics", *Ap&SS Proceedings*, Springer, pp. 115-165
- Barden, M., et al. 2005, *ApJ*, 635, 959
- Baugh, C. M. 2006, *Reports on Progress in Physics*, 69, 3101
- Bergvall, N., Zackrisson, E., & Caldwell, B. 2009, (astro-ph/0909.4296)
- Bell E. F., Zheng X. Z., Papovich C., Borch A., Wolf C., Meisenheimer K., 2007, *ApJ*, 663, 834
- Birnbom, Y., & Dekel, A. 2003, *MNRAS*, 345, 349
- Brooks, A. M., Governato, F., Quinn, T., Brook, C. B., & Wadsley, J. 2009, *ApJ*, 694, 396
- Bullock, J.S., Dekel, A., Kolatt, T.S., Kravtsov, A.V., Klypin, A.A., Porciani, C., & Primack, J.R. 2001, *ApJ*, 555, 240
- Ceverino, D., & Klypin, A. 2009, *ApJ*, 695, 292
- Ceverino, D., Dekel, A., & Bournaud, F. 2009, preprint (astro-ph/0907.3271)
- Conroy, C., Gunn, J. E., & White, M. 2009a, *ApJ*, 699, 486
- Conroy, C., White, M., & Gunn, J. E. 2009b, preprint (astro-ph/0904.0002)
- Dalla Vecchia C., Schaye J., 2008, *MNRAS*, 387, 1431
- Damen, M., Labbé, I., Franx, M., van Dokkum, P. G., Taylor, E. N., & Gawiser, E. J. 2009, *ApJ*, 690, 937
- Dekel, A., & Silk, J. 1986, *ApJ*, 303, 39
- Dubois, Y., & Teyssier, R. 2008, *A&A*, 477, 79
- Ferland, G.J., Korista, K.T., Verner, D.A., Ferguson, J.W., Kingdon, J.B., & Verner, E.M. 1998, *PASP*, 110, 761
- Firmani, C., Avila-Reese, V. & Rodríguez-Puebla, A. 2009, submitted
- Fontanot, F., De Lucia, G., Monaco, P., Somerville, R. S., & Santini, P. 2009, preprint (astro-ph/0901.1130)
- Franco, J., & Cox, D. P. 1986, *PASP*, 98, 1076
- Gerritsen, I.P.E., & Icke, V. 1997, *A&A*, 325, 972
- Gnedin, N. Y., Tassis, K., & Kravtsov, A. V. 2009, *ApJ*, 697, 55
- Gibson, B. K., Courty, S., Sánchez-Blázquez, P., Teyssier, R., House, E. L., Brook, C. B., & Kawata, D. 2009, *IAU Symposium*, 254, 445
- Governato, F., et al. 2004, *ApJ*, 607, 688
- Governato, F., Willman, B., Mayer, L., Brooks, A., Stinson, G., Valenzuela, O., Wadsley, J., & Quinn, T. 2007, *MNRAS*, 374, 1479
- Haardt, F., & Madau, P. 1996, *ApJ*, 461, 20
- Heitsch, F., Mac Low, M.-M., & Klessen, R. S. 2001, *ApJ*, 547, 280
- Hernández, X., Avila-Reese, V., & Firmani, C. 2001, *MNRAS*, 327, 329
- Katz, N. 1992, *ApJ*, 391, 502
- Katz, N., Weinberg, D. H., & Hernquist, L. 1996, *ApJS*, 105, 19
- Kennicutt, R.C. 1998, *ApJ*, 498, 541
- Kereš, D., Katz, N., Weinberg, D.H., & Davé, R. 2005, *MNRAS*, 363, 2
- Klessen, R. S., Heitsch, F., & MacLow, M. M. 2000, *ApJ*, 535, 887
- Klypin, A., & Holtzman, J. 1997, preprint (astro-ph/9712217)
- Klypin, A.A., Kravtsov, A.V., Bullock, J.S., & Primack, J.R. 2001, *ApJ*, 554, 903
- Kravtsov, A.V., Klypin, A.A., & Khokhlov, A.M., 1997, *ApJS*, 111, 73
- Kravtsov, A.V. 1999, PHD thesis, New Mexico State University
- Kravtsov, A.V. 2003, *ApJ(Letters)*, 590, 1
- Kravtsov, A.V., Nagai, D., & Vikhlinin, A.A. 2005, *ApJ*, 625, 588
- Krumholz, M. R., & McKee, C. F. 2005, *ApJ*, 630, 250
- Mac Low, M.-M., & Klessen, R. S. 2004, *Reviews of Modern Physics*, 76, 125
- Martin, C. L., & Kennicutt, R. C., Jr. 2001, *ApJ*, 555, 301
- Mayer, L., Governato, F., & Kaufmann, T. 2008, *Advanced Science Letters*, 1, 7
- Miller, G.E., & Scalo, J.M. 1979, *ApJS*, 41, 513
- Navarro, J. F., & White, S. D. M. 1993, *MNRAS*, 265, 271
- Navarro, J.F., Frenk, C.S., & White, S.D.M. 1997, *ApJ*, 490, 493
- Noeske K. G., et al., 2007, *ApJ*, 660, L47
- Okamoto, T., Jenkins, A., Eke, V. R., Quilis, V., & Frenk, C. S. 2003, *MNRAS*, 345, 429
- Okamoto, T., Eke, V. R., Frenk, C. S., & Jenkins, A. 2005, *MNRAS*, 363, 1299
- Ostriker, E. C., Gammie, C. F., & Stone, J. M. 1999, *ApJ*, 513, 259
- Pedrosa, S., Tissera, P. B., & Scannapieco, C. 2009, *MNRAS*, 395, L57
- Persic, M., Salucci, P., & Stel, F. 1996, *MNRAS*, 281, 27
- Rasera, Y., & Teyssier, R. 2006, *A&A*, 445, 1
- Rhee, G., Valenzuela, O., Klypin, A., Holtzman, J., & Moorthy, B. 2004, *ApJ*, 617, 1059
- Robertson, B., Bullock, J.S., Cox, T.J., Di Matteo, T., Hernquist, L., Springel, V., & Yoshida, N. 2006, *ApJ*, 645, 986
- Rosas-Guevara, Y, Vázquez-Semadeni, E., Gómez, G. C., Jappsen, A.-K. 2010, *MNRAS*, submitted
- Sackett, P. D. 1997, *ApJ*, 483, 103
- Saitoh, T. R., Daisaka, H., Kokubo, E., Makino, J., Okamoto, T., Tomisaka, K., Wada, K., & Yoshida, N. 2008, *PASJ*, 60, 667
- Scannapieco, C., Tissera, P. B., White, S. D. M., & Springel, V. 2006, *MNRAS*, 371, 1125
- Scannapieco, C., Tissera, P. B., White, S. D. M., & Springel, V. 2008, *MNRAS*, 389, 1137
- Sommer-Larsen, J., & Dolgov, A. 2001, *ApJ*, 551, 608
- Sommer-Larsen, J., Götz, M., & Portinari, L. 2003, *ApJ*, 596, 47
- Somerville, R. S., et al. 2008, *ApJ*, 672, 776

- Springel, V., & Hernquist, L. 2003, MNRAS, 339, 289
Springel, V., & Hernquist, L. 2005, ApJ, 622, 9
Stinson, G., Seth, A., Katz, N., Wadsley, J., Governato, F., & Quinn, T. 2006, MNRAS, 373, 1074
Stinson, G. S., Dalcanton, J. J., Quinn, T., Gogarten, S. M., Kaufmann, T., & Wadsley, J. 2009, MNRAS, 395, 1455
Swaters, R. A., Sancisi, R., van Albada, T. S., & van der Hulst, J. M. 2009, A&A, 493, 871
Thacker, R.J., & Couchman, H.M.P. 2000, ApJ, 545, 728
Valenzuela, O., Rhee, G., Klypin, A., Governato, F., Stinson, G., Quinn, T., & Wadsley, J. 2007, ApJ, 657, 773
Vázquez-Semadeni, E., Ballesteros-Paredes, J. & Klessen, R. S. 2003, ApJ, 585, L131
Vázquez-Semadeni, E., Kim, J., & Ballesteros-Paredes, J. 2005, ApJ, 630, L49
Vázquez-Semadeni, E., Colín, P., Gómez, G.C., & Watson, A.W. 2010, ApJ, submitted
van Dishoeck, E. F., & Black, J. H. 1988, ApJ, 334, 771
Weinberg, D. H., Colombi, S., Davé, R., & Katz, N. 2008, ApJ, 678, 6
White, S. D. M., & Rees, M. J. 1978, MNRAS, 183, 341
Wyder, T. K., et al. 2009, ApJ, 696, 1834
Yepes, G., Kates, R., Khokhlov, A., & Klypin, A. 1997, MNRAS, 284, 235
Zavala, J., Okamoto, T., & Frenk, C. S. 2008, MNRAS, 387, 364
Zheng X. Z., Bell E. F., Papovich C., Wolf C., Meisenheimer K., Rix H.-W., Rieke G. H., Somerville R., 2007, ApJ, 661, L41